Science Arts & Métiers (SAM)
is an open access repository that collects the work of Arts et Métiers Institute of Technology researchers and makes it freely available over the web where possible.

This is an author-deposited version published in: https://sam.ensam.eu
Handle ID: .http://hdl.handle.net/10985/21621

To cite this version :

Lei SHI, Yefang WANG, Olivier COUTIER-DELGOSHA, Annie-Claude BAYEUL-LAINÉ - Numerical investigations on transitional flows around forward and reversed hydrofoils - European Journal of Mechanics - B/Fluids - Vol. 85, p.24-45 - 2021

Any correspondence concerning this service should be sent to the repository Administrator : scienceouverte@ensam.eu

Numerical investigations on transitional flows around forward and reversed hydrofoils

Lei Shi[1,2,*], Yefang Wang[2], Annie-Claude Bayeul-Lainé[1], Olivier Coutier-Delgosha[1,3]

[1]Arts et Métiers ParisTech, ONERA, CNRS, Univ. Lille, Centrale Lille, UMR 9014-LMFL-Laboratoire de Mécanique des Fluides de Lille-Kampé de Fériet, F-59000 Lille, France

[2]Research Centre of Fluid Machinery Engineering and Technology, Jiangsu University, China

[3]Kevin T. Crofton Department of Aerospace and Ocean Engineering, Virginia Tech, Blacksburg, VA 24060, USA

[*]Corresponding author e-mail: mumuyedda@126.com

Abstract

The laminar-turbulence transition phenomenon widely exists on the surface of many energy equipment, which is deserved to be studied because of the complex mechanics and some induced undesirable consequences. The goal of present work is to investigate the transitional flows around the forward and reversed hydrofoils at different incidences using the SST γ-$\widetilde{Re}_{\theta t}$ transition model, with special emphasis on the dynamics of the transition. The effect of inflow turbulence condition is considered initially. Then, the difference between the original SST k-ω model and SST γ-$\widetilde{Re}_{\theta t}$ transition model is analyzed, in terms of the near-wall velocity profiles and flow morphology. Afterwards, the change of the transition with the incidence for the reversed hydrofoil is clarified in detail. The primary results show that the flow separation near the sharp leading edge where the reverse dynamic vortex (RDV) appears makes the contribution to the transition. The size of RDV is much larger than laminar separation bubble (LSB) over the forward hydrofoil and it forms near the leading edge earlier. Moreover, the transition locations are mapped both for the forward and reversed hydrofoils. Finally, the effect of Reynolds number on the transition process for the reversed hydrofoil is presented. It is believed that this work can deep the understandings of the transition, especially for the reversed hydrofoils.

Keywords: numerical simulations; transition model; inflow turbulence; reversed hydrofoil; Reynolds number

1. Introduction

The rotors with complex kinematics, submitted to some engineering applications including the high-speed helicopters, the large-scale vertical axis wind turbine (VAWT) and underwater propeller thruster, always experience a large variation of incidences, resulting in the significant change of the overall performance for both the single blade and rotating system. As is shown in figure 1, in a specific cycle of the foil movement, the blade always undergoes the retreating and advancing sides, representing different displacements of the configuration. When the local free-stream velocity exceeds the rotor rotational velocity, the reverse flow emerges at blade stations, leading to the flow that travels from the geometrical trailing edge to the geometrical leading edge, which can bring about the drag increase, downward-acting lift and a large pitching moment [1-2]. Most aforementioned investigations mainly concentrate on the unsteady and time-averaged behavior of turbulent flows around the rotor blade as it passes through the advancing side with the forward configuration, but the detailed understandings in physics of flows around the reversed blade is still infrequent.

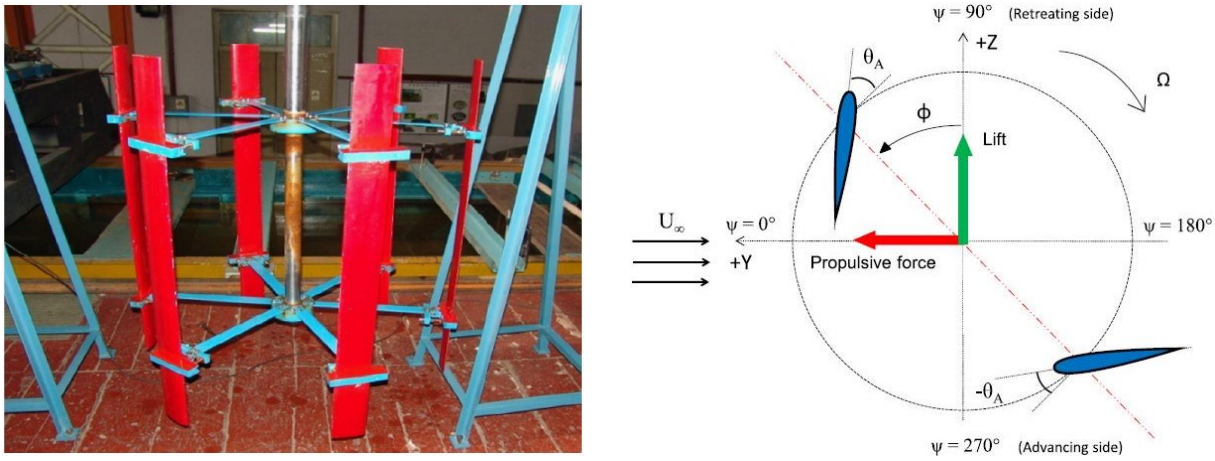

(a) (b)

Figure 1 Applications of reversed foils. (a) Variable-pitch vertical axis turbine; (b) Cycloidal rotor.

The LSB formed over the foil surface, mainly induced by the laminar boundary layer separation subjected to the strong adverse pressure gradient and the reattachment of the turbulent boundary layer, has some adverse effects, involving the flow oscillation, resultant noise and vibration and abrupt stall due to the bubble bursting. Additionally, the location, appearance and intensity of LSB are strongly affected by some important parameters, e.g. Reynolds number [3-4], attack angle [5-6], free-stream turbulence intensity [7-8], foil geometry and elasticity [9-10] and surface roughness [11]. It is well known that the laminar-turbulence transition phenomenon often occurs in the engineering practice, but the available information with respect to the near-wall flows obtained by experiments is still challenging due to the difficulties in accessing to the thin boundary layer. Therefore, computational fluid dynamics (CFD), predominantly Reynolds Averaged Navier-Stokes (RANS) methods, but also large eddy simulation (LES), have made a great progress recently and they can provide a deep insight on the transitional flows. However, the conventional RANS model without considering the transition process is only used to resolve the fully turbulent flows while the transition model

coupled with the standard turbulence model can have a better prediction of the endwall flows, in terms of the velocity profiles, pressure and skin friction coefficients. One of the widely-used transition models is shear stress transport (SST k-ω) turbulence model coupled with γ-$\widetilde{Re}_{\theta t}$ transition model firstly proposed by Menter [12-14], in which the production and destruction terms in turbulence kinetic energy equation is modified by the introduction of effective intermittency. This model has been successfully applied to predict the hydrodynamic/aerodynamic performance of the open water propeller [15-16] and wind turbine [17]. But when extending the applicability of RANS transition models to the low Reynolds number flows, it is observed that the lag elliptic blending model [18] and k-k_L-ω model [19] have a better prediction in the correct transition physics and secondary flow near the surface respectively. The Spalart-Allmaras (SA) transition model is the other one developed based on the similar concept of the SST γ-$\widetilde{Re}_{\theta t}$ model, which has already achieved a good reputation in simulating the aerodynamic transitional flows [20-21]. Other improved transition models and the transition modeling strategies can refer to some related references [22-25]. Moreover, large eddy simulation which consists of modelling the more universal small-scales while the motions of large scales are computed explicitly is a promising tool but remains extremely costly in computer resources for the configuration with large dimension or at high Reynolds number. For some specific examples, Almutairi et al. [26] used LES model to investigate the dynamics of LSB over an airfoil near stall conditions and the main conclusion is that the flow oscillation can be ascribed to the quasi-periodic bursting and reforming of LSB. Benton and Visbal [27] studied the onset of dynamic stall at a high and transitional Reynolds number via wall-resolved LES and they found that the roll-up process of LSB can result in the onset of dynamic stall which is sensitive to the Reynolds number strongly. Simultaneously, Asada and Kawai [28] also applied wall-resolved LES to clarify the shear layer instability by detecting the high frequency at LSB near the leading edge and low frequency at the turbulent separation near the trailing edge. Many other works regarding the dynamic stall associated with the LSB obtained by LES methodology can be found in references [29-30]. It has no doubt that the LES can capture more detailed flow structures either near the solid wall or in the vortex shedding region, but the large requirement of the mesh nodes, the small time-step and long-time sampling makes it unfeasible for most engineering turbulent flows.

The reversed foil has quite different blade loading and vortex structure evolution with that for the forward configuration. For the static reversed airfoil, three reverse flow wake regimes including the slender body vortex shedding, turbulent and deep stall vortex shedding are identified [31], and the dynamics depend on the foil geometry significantly which shows that the flow separation near the foil surface is delayed for the elliptical airfoil, causing the decrease of the pressure drag [32-33]. When given to the Reynolds number effect, it is observed that the thin foil is not sensitive to the increase of Reynolds number compared with the thick foil and the blade loads would decrease as the Reynolds number increases in a specific range of the attack angle [34-35]. Marchand et al. [36] observed that the occurrence of lift discontinuity is at 0° for the hydrofoil in reverse flow, as a consequence of the leading edge separation bubble and asymmetrical boundary layers, which can't be detected by the original RANS turbulence model. With the consideration of dynamic stall in reverse flow, the distinctive vortex structures are reverse flow dynamic stall vortices (RFDSVs) and the dynamic stall has a close correlation with the Reynolds number, pitching frequency, mean pitch angle and pitch amplitude [37], yaw angle [38] and foil shape [39]. Due to the massive flow separation and vortex shedding, the

reverse flow can lead to the unsteady loading, vibration and fatigue. Therefore, Clifford et al. [40] used the plasma actuators attached on the foil leading edge and trailing edge to evaluate which mode is more effective and the results show that large-scale wake structures are suppressed and the pressure fluctuation is reduced as the plasma actuators are placed at the trailing edge, while they can reduce the separation region and increase the lift coefficient when they are located at the leading edge.

In the present work, with the consideration of transition onset, the SST γ-$\widetilde{Re}_{\theta t}$ transition model is employed to investigate the transitional flows around the stationary forward and reversed hydrofoils. The results obtained by the SST *k*-*ω* model with/without transition model are compared with the existing experiments. Various attack angles from a negative value (-5°) to a positive one (14°) are studied and the effect of Reynolds number on the reverse flows is also be taken into consideration. The main attention is paid to the transition locations induced by the LSB under various working conditions. It is believed that this work can provide a deep insight on the transitional flows for the reversed hydrofoil, bringing about a better design of the aerodynamic/hydrodynamic devices.

2. Turbulence modeling

2.1 Incompressible Navier-Stokes equations

The unsteady incompressible viscous flow is performed in this work. The conservation equations of mass and momentum are given by

$$\frac{\partial u_j}{\partial x_j} = 0 \tag{1}$$

$$\frac{\partial u_i}{\partial t} + u_j \frac{\partial u_i}{\partial u_j} = -\frac{1}{\rho}\frac{\partial p}{\partial x_i} + \nu \frac{\partial^2 u_i}{\partial x_j \partial x_j} \tag{2}$$

where u, ρ, p, ν and t are velocity, density, pressure, kinetic viscosity and time. i and j are Einstein notations.

2.2 SST *k*-*ω* turbulence model

The choice of SST *k*-*ω* turbulence model is due to the capability of resolving the flows with strong pressure gradients and flow separation [41]. It combines the *k*-*ω* model which can be used to solve the near-wall flows and *k*-*ε* model responsible for the outside free-stream flows. The SST *k*-*ω* is a two-equation model including the *k* equation and *ω* equation, given by

$$\frac{\partial k}{\partial t} + u_j \frac{\partial k}{\partial x_j} = P_k - \beta^* k\omega + \frac{\partial}{\partial x_j}\left[(\nu + \sigma_k \nu_t)\frac{\partial k}{\partial x_j}\right] \tag{3}$$

$$\frac{\partial \omega}{\partial t} + u_j \frac{\partial \omega}{\partial x_j} = \frac{\alpha}{\nu_t} P_k - \beta\omega^2 + \frac{\partial}{\partial x_j}\left[(\nu + \sigma_\omega \nu_t)\frac{\partial \omega}{\partial x_j}\right] + 2(1 - F_1)\frac{\sigma_{\omega 2}}{\omega}\frac{\partial k}{\partial x_j}\frac{\partial \omega}{\partial x_j} \tag{4}$$

Then, the kinematic eddy viscosity is used to closure these two equations, shown as follows

$$\nu_t = \frac{a_1 k}{max(a_1\omega, SF_2)} \tag{5}$$

Additionally, some important parameters in these two equations are expressed by

$$P_k = min\left(\tau_{ij}\frac{\partial u_i}{\partial x_j}, 10\beta^* k\omega\right) \tag{6}$$

$$\tau_{ij} = 2\nu_t S_{ij} - \frac{2}{3}\delta_{ij}k \tag{7}$$

$$S = \sqrt{2S_{ij}S_{ij}} \quad S_{ij} = \frac{1}{2}\left(\frac{\partial u_i}{\partial x_j} + \frac{\partial u_j}{\partial x_i}\right) \tag{8}$$

$$F_1 = tanh\left\{\left\{min\left[max\left(\frac{\sqrt{k}}{\beta^*\omega y}, \frac{500\nu}{y^2\omega}\right), \frac{4\rho\sigma_{\omega 2}k}{CD_{k\omega}y^2}\right]\right\}^4\right\} \tag{9}$$

$$F_2 = tanh\left[\left[max\left(\frac{2\sqrt{k}}{\beta^*\omega y}, \frac{500\nu}{y^2\omega}\right)\right]^2\right] \tag{10}$$

$$CD_{k\omega} = max\left(2\rho\sigma_{\omega 2}\frac{1}{\omega}\frac{\partial k}{\partial x_i}\frac{\partial \omega}{\partial x_i}, 10^{-10}\right) \tag{11}$$

where τ_{ij} is the shear stress and y is the near-wall distance. Moreover, the values of the variables are calculated by $\varphi = \varphi_1 F_1 + \varphi_2(1 - F_1)$ and the magnitudes of the components are listed in Table 1.

Table 1 Values of some parameters in SST *k-ω* turbulence model

α_1	5/9	α_2	0.44
β_1	0.075	β_2	0.0828
σ_{k1}	0.85	σ_{k2}	1.0
$\sigma_{\omega 1}$	0.50	$\sigma_{\omega 2}$	0.856
β^*	0.09	a_1	0.31

2.3 The γ-$\widetilde{Re}_{\theta t}$ transition model

When it comes to the γ- $\widetilde{Re}_{\theta t}$ transition model [12-13], two equations, namely intermittency γ and transition momentum thickness Reynolds number $\widetilde{Re}_{\theta t}$, are given by

$$\frac{\partial \gamma}{\partial t} + \frac{\partial(u_j\gamma)}{\partial x_j} = P_\gamma - E_\gamma + \frac{\partial}{\partial x_j}\left[\left(\nu + \frac{\nu_t}{\sigma_\gamma}\frac{\partial \gamma}{\partial x_j}\right)\right] \tag{12}$$

$$\frac{\partial \widetilde{Re}_{\theta t}}{\partial t} + \frac{\partial(u_j\widetilde{Re}_{\theta t})}{\partial x_j} = P_{\theta t} + \frac{\partial}{\partial x_j}\left[(\nu + \nu_t)\sigma_{\theta t}\frac{\partial \widetilde{Re}_{\theta t}}{\partial x_j}\right] \tag{13}$$

where the production source term P_γ is defined as follows

$$P_\gamma = F_{length}C_{a1}S[\gamma F_{onset}]^{0.5}(1 - C_{e1}\gamma) \tag{14}$$

$$F_{onset} = max(F_{onset2} - F_{onset3}, 0) \tag{15}$$

$$F_{onset2} = min(max(F_{onset1}, F_{onset1}^4), 2.0) \tag{16}$$

$$F_{onset3} = max\left(1 - \left(\frac{R_T}{2.5}\right)^3, 0\right) \tag{17}$$

$$F_{onset1} = \frac{Re_v}{2.913Re_{\theta c}} \tag{18}$$

$$Re_v = \frac{y^2 S}{v} \tag{19}$$

$$R_T = \frac{k}{v\omega} \tag{20}$$

where S is the strain rate magnitude, F_{length} is an empirical correlation that controls the length of the transition region, F_{onset} controls the transition onset location, and $Re_{\theta c}$ is a critical

Reynolds number at which the intermittency starts to increase in the boundary layer. Both F_{length} and $Re_{\theta c}$ correlate with $\widetilde{Re}_{\theta t}$.

The destruction source term E_γ can be written by

$$E_\gamma = C_{a2}\Omega\gamma F_{turb}(C_{e2}\gamma - 1) \tag{21}$$

where Ω is the vorticity magnitude and F_{turb} is used to disable the destruction sources outside of a laminar boundary layer or in the viscous sublayer, which can be defined as follows

$$F_{turb} = e^{-\left(\frac{R_T}{4}\right)^4} \tag{22}$$

For the production source term $P_{\theta t}$, it follows the formulation presented by

$$P_{\theta t} = C_{\theta t}\frac{\rho}{t}\left(Re_{\theta t} - \widetilde{Re}_{\theta t}\right)(1.0 - F_{\theta t}) \tag{23}$$

$$t = \frac{500v}{U^2} \tag{24}$$

$$F_{\theta t} = min\left(max\left(F_{wake}e^{-\left(\frac{y}{\sigma}\right)^4}, 1.0 - \left(\frac{\gamma - 1/C_{e2}}{1.0 - 1/C_{e1}}\right)^2\right), 1.0\right) \tag{25}$$

$$\theta_{BL} = \frac{\widetilde{Re}_{\theta t}v}{U};\ \ \delta_{BL} = \frac{15}{2}\theta_{BL};\ \ \delta = \frac{50\Omega y}{U}\delta_{BL} \tag{26}$$

$$Re_\omega = \frac{\omega y^2}{v};\ \ F_{wake} = e^{-\left(\frac{Re_\omega}{1E+5}\right)^2} \tag{27}$$

where the source term $P_{\theta t}$ is used to force $\widetilde{Re}_{\theta t}$ to match the local value of $Re_{\theta t}$ calculated from an empirical correlation outside the boundary layer. The blending function, $F_{\theta t}$, turns off the source term in the boundary layer and allow $\widetilde{Re}_{\theta t}$ to diffuse in the free-stream. Therefore, it is equal to one in the boundary layer and zero in the free-stream. The empirical correlation of $Re_{\theta t}$ is on the basis of turbulence intensity Tu and the stream-wise pressure gradient λ_θ.

To correct the deficiency that it takes a long time for turbulent kinetic energy k to have a large value that causes the boundary layer reattachment at low free-stream turbulence intensities, the modification to the intermittency for predicting the flow-induced transition is

$$\gamma_{sep} = min\left(s_1 max\left[0, \left(\frac{Re_v}{3.235Re_{\theta c}}\right) - 1\right]F_{reattach}, 2\right)F_{\theta t} \tag{28}$$

$$F_{reattach} = e^{-\left(\frac{R_T}{20}\right)^4} \tag{29}$$

$$\gamma_{eff} = max(\gamma, \gamma_{sep}) \tag{30}$$

2.4 Coupling with the SST *k-ω* turbulence model

The implementation of the transition equations into the SST *k-ω* model is by the introduction of an effective intermittency γ_{eff}, which only modifies the turbulence production and diffusion terms shown as follows

$$\hat{P}_k = \gamma_{eff}P_k, \hat{D}_k = min\left(max\left(\gamma_{eff}, 0.1\right), 1.0\right)\beta^* k\omega \tag{31}$$

where P_k and $\beta^* k\omega$ are the source terms of turbulence production and diffusion in SST *k-ω* model. The modification of blending function F_{1mod} is necessary because it can switch potentially from 1 to 0 in the center of laminar boundary layer. The modified blending function is defined as follows

$$F_{1mod} = max\left(F_{1orig}, F_3\right) \tag{32}$$

$$F_3 = e^{-\left(\frac{R_y}{120}\right)^8}; \quad R_y = \frac{y\sqrt{k}}{v} \tag{33}$$

where F_{1orig} is the original blending function of the SST k-ω turbulence model. The specific values of some constants in transition model are presented in Table 2.

Table 2 Values of some parameters in γ-$\widetilde{Re}_{\theta t}$ transition model

C_{a1}	2.0	C_{a2}	0.06
C_{e1}	1.0	C_{e2}	50
σ_γ	1.0	$\sigma_{\theta t}$	20
$C_{\theta t}$	0.03	s_1	2.0

3. Flow configuration and numerical setup

3.1 Computational domain and mesh generation

The two-dimensional stationary hydrofoil used in the present work is NACA66312 which has a chord length of 0.15m and the corresponding Reynolds number is 7.5×10^5. The origin coordinate is placed at the leading edge of the hydrofoil at 0°. Then, the incidence changes from -5° to 14° around a fixed pivot located at 0.25c (c is the chord length), both for the forward and reversed hydrofoils. Similar with the experimental setup, the computational configuration has a height of 0.192mm while it extends 2c from the leading edge and 5c from the trailing edge, which is displayed in figure 2.

For the mesh generation, the high-quality structured meshes are used for all the tested cases. Due to the transition phenomenon existing on the foil surface, the mesh distribution near the wall is quite critical for the transition locations. Therefore, the refined mesh with the stretch ratio of 1.02 from the wall to outside region is adopted. To check the mesh influence on the foil performance, the mesh independence results for the forward hydrofoil at 2° are presented in Table 3 (C_l is the lift coefficient defined by $C_l=F_y/(0.5*\rho*U_0^2*c)$, where F_y is the force in y direction and U_0 is the free-stream velocity, and drag coefficient C_d is defined as $C_d=F_x/(0.5*\rho*U_0^2*c)$, where F_x is the force in x direction). By the comparisons with the experiments, it concludes that the maximal error is below 2% and the discrepancy of the lift coefficient obtained by mesh 3 and mesh 4 is quite close. In addition, as is listed in Table 4, the results obtained by different meshes at 8° are also displayed. The discrepancy of predicted lift coefficient with the experiments is below 4% and it seems that there is no much difference between mesh 2 and mesh 3. The error between the numerical results and experiments is possibly caused by the wall roughness, three-dimensional effect and numerical uncertainty. The pressure coefficient $C_p=p/(0.5*\rho*U_0^2)$ (p is the pressure) in figure 3a shows that the results of different meshes are almost the same. However, based on the distribution of skin friction coefficient $C_f=\tau/(0.5*\rho*U_0^2)$ (τ is the wall shear stress) displayed in figure 3b, it is observed that the predictive transition location near the leading edge is quite similar for mesh 2 and 3. Therefore, to get a better transition location, it is necessary to keep the maximal y^+ below 1.5 for all the tested cases.

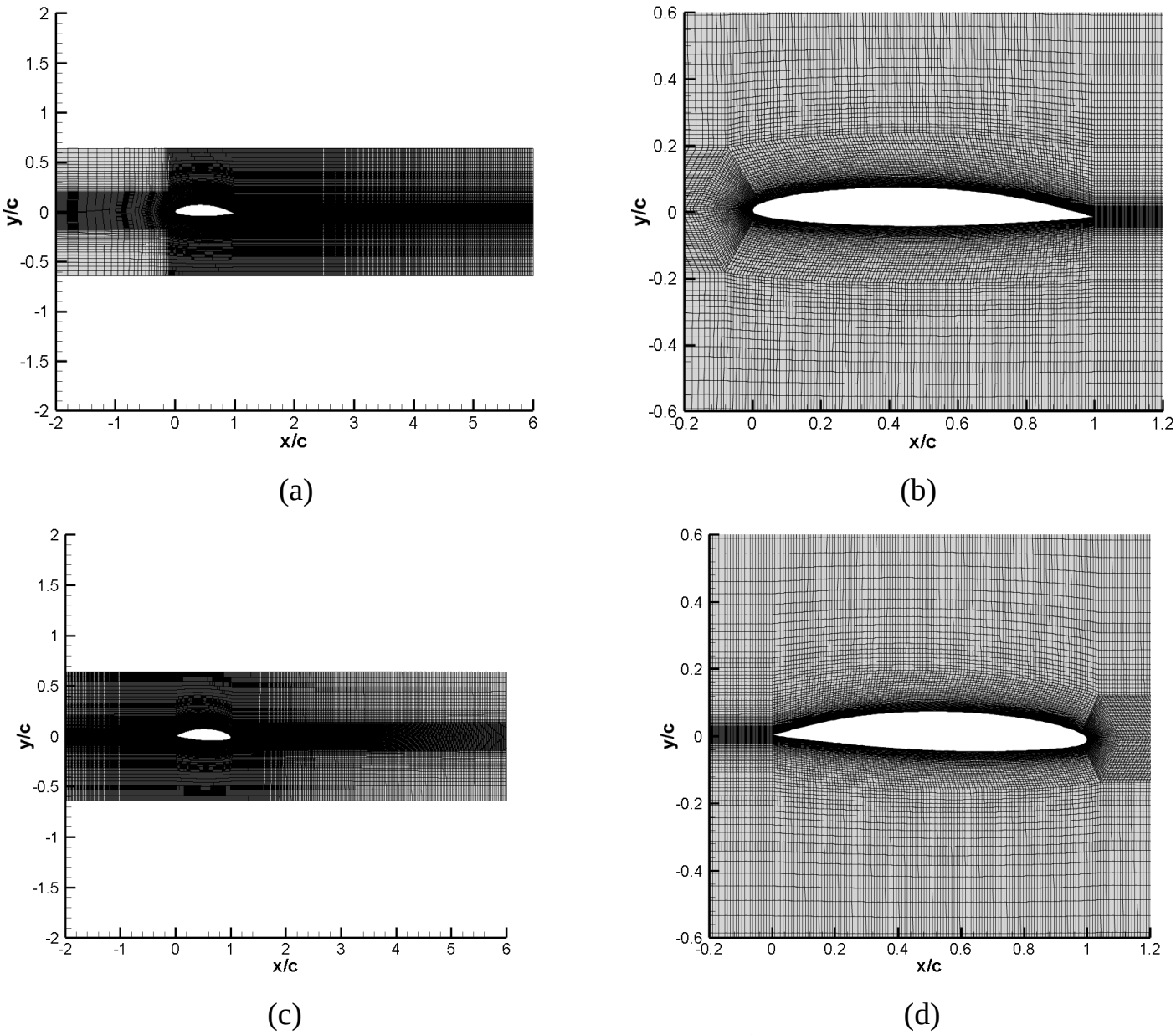

Figure 2 Computational domain and mesh distribution at 1°. (a) Goble mesh for the forward hydrofoil; (b) Mesh near the forward foil surface; (c) Goble mesh for the reversed hydrofoil; (d) Mesh near the reversed foil surface.

Table 3 Influence of the mesh on hydrofoil performance at 2°

	Total nodes	y_{max}^+	Lift coefficient C_l	Error (%)	Drag coefficient C_d
Mesh 1	153,470	2.46	0.58786	1.22	0.00645
Mesh 2	182,650	1.93	0.58623	1.49	0.00637
Mesh 3	239,570	1.25	0.58529	1.65	0.00630
Mesh 4	301,190	1.08	0.58496	1.71	0.00630
EXP	--	--	0.59512	--	--

Table 4 Influence of the mesh on hydrofoil performance at 8°

	Total nodes	y_{max}^+	Lift coefficient C_l	Error (%)	Drag coefficient C_d
Mesh 1	226,540	3.39	1.1099	3.55	0.020685
Mesh 2	258,870	1.38	1.1118	3.38	0.020743
Mesh 3	324,950	1.27	1.1126	3.31	0.020794
EXP	--	--	1.1507		--

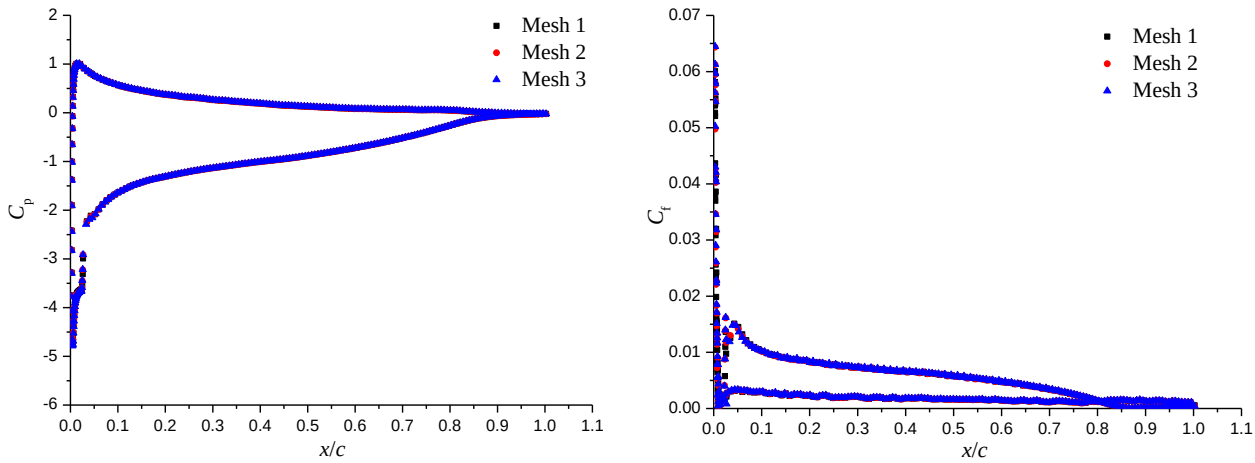

(a) (b)

Figure 3 Distributions of pressure and skin friction coefficients for different meshes at 8°. (a) Pressure coefficients; (b) Skin friction coefficients.

3.2 Boundary conditions and numerical setup

For the boundary conditions, the classical ones are used as follows: the constant velocity U_0=5 m/s is imposed on the inlet section while the static pressure p=0 Pa is assigned on the outlet section, which is consistent with the experimental setup [42]. Then, the side-walls in spanwise direction are regarded as the symmetrical plains and the no-slip wall condition is employed for the foil surface. The top-wall and bottom-wall are also treated as the symmetrical boundary conditions, for the reason that the slight blockage induced by the development of the boundary layers on these faces should be avoided. Therefore, the top-wall and bottom-wall of the cavitation tunnel is often slightly divergent. Actually, the results obtained by the symmetrical planes and no-slip walls have no difference.

In the solver control, the high-resolution scheme is adopted for the advection scheme while the second order backward Euler is applied to the transient scheme. The maximal loops for each timestep is 10 because it takes more time to achieve the convergence for the transition model, and the convergence target is set as 1×10^{-5}. Furthermore, the timestep is given as 10^{-5}s, which can get a root-mean-square (RSM) courant number below 1. As the initial condition, the results of the steady computations are used for the unsteady simulations. Finally, a long-time sampling is necessary to get a steady or quasi-steady result.

4. Results and discussion

4.1 Effect of inflow turbulence condition

On the basis of the previous investigations, it concludes that the inflow turbulence condition has great influence on the dynamics of LSB and transition locations, which can further affect the hydrodynamic performance of the hydrofoils. Therefore, the inflow turbulence condition effect is presented in this section, by the inflow turbulence intensity *Tu* and eddy viscosity ratio μ_t/μ (where μ_t is the eddy viscosity and μ is the dynamic viscosity). Table 5 lists the hydrofoil performance under different inflow turbulence intensity conditions. It is found that increasing the turbulence intensity has no great impact on the hydrofoil performance. Indeed, as is shown in figure 4, the transition locations both on the upper and lower surfaces predicted by different turbulence intensity are very close. Figure 5 plotted the distributions of pressure and skin friction coefficients for various turbulence intensity conditions and the results are very similar. It can capture the transitions on the pressure and suction sides. According to the experimental setup [42], the measured inflow turbulence intensity is nearly 3%, which is employed finally to all the cases.

Table 5 Effect of inflow turbulence intensity on hydrofoil performance

Turbulence intensity (%)-eddy viscosity ratio	Lift coefficient C_l	Error (%)	Drag coefficient C_d
1-10	0.589	1.01	0.00632
3-10	0.585	1.68	0.00630
5-10	0.589	1.01	0.00630
EXP	0.595	--	--

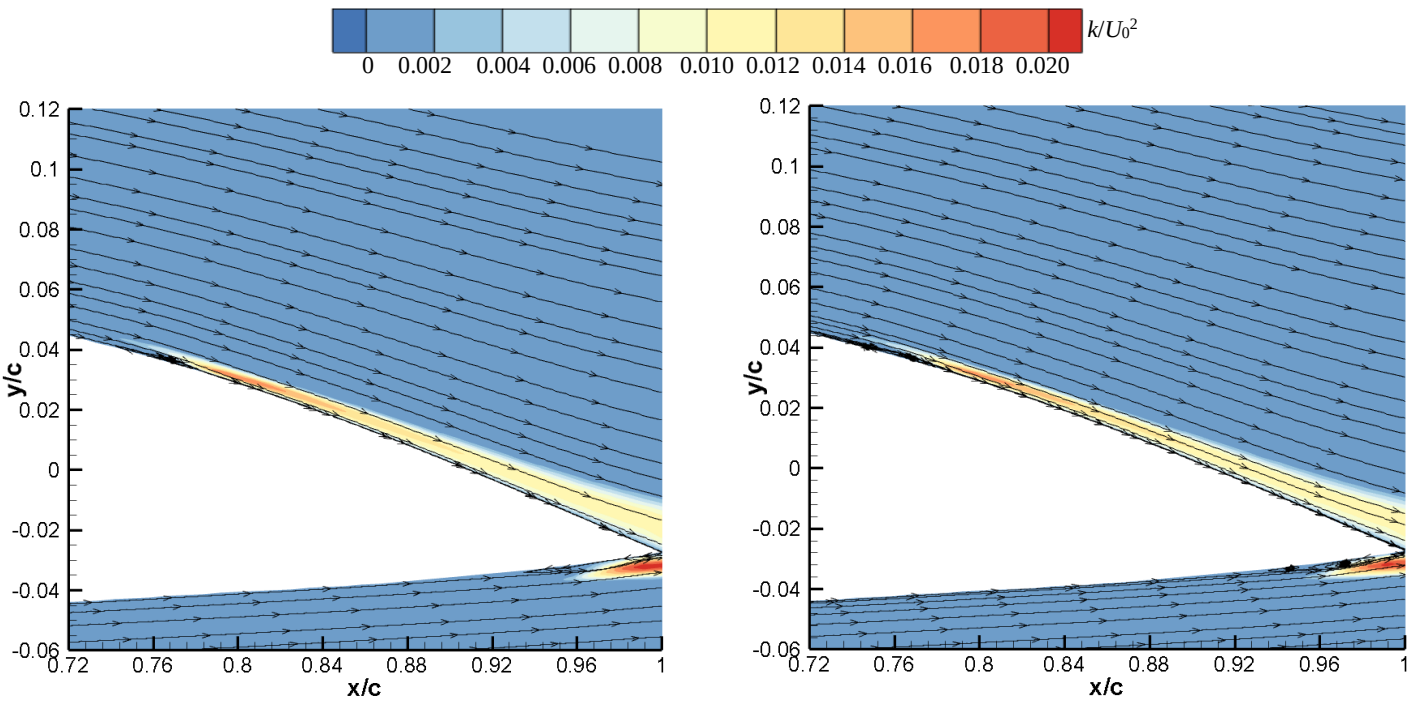

(a) (b)

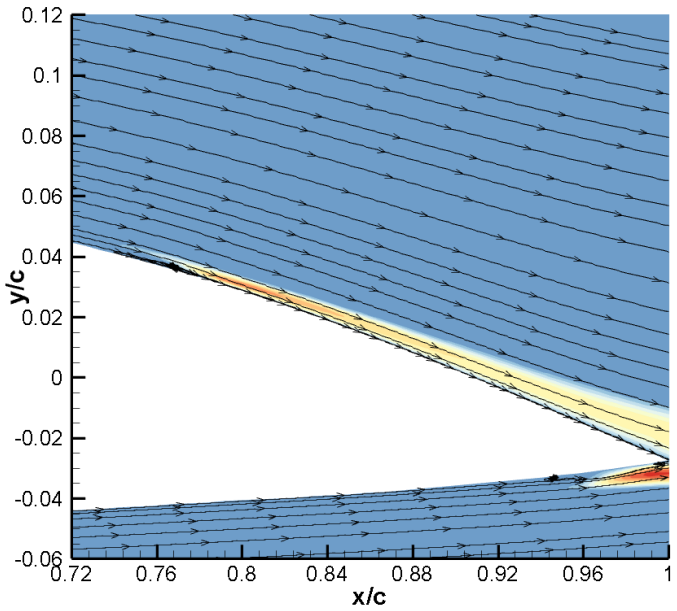

(c)

Figure 4 Distributions of turbulence kinetic energy with the streamlines at 2°. (a) 1-10; (b) 3-10; (c) 5-10.

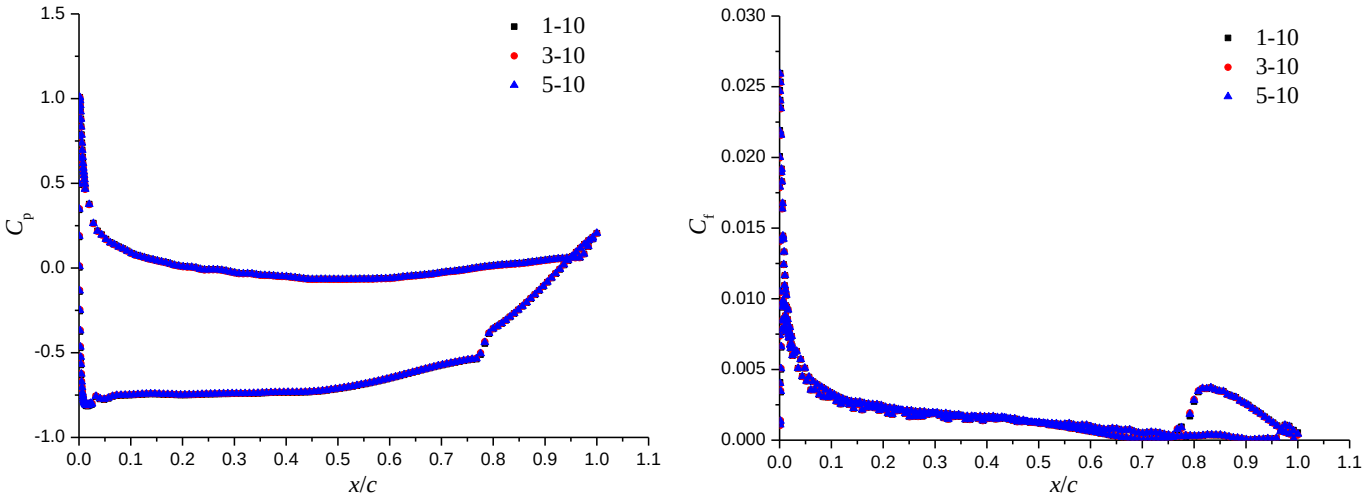

(a) (b)

Figure 5 Distributions of pressure and skin fiction coefficients at 2°. (a) Pressure coefficient; (b) Skin friction coefficient.

Then, the effect of eddy viscosity ratio is also considered and the predictive hydrofoil performance are displayed in Table 6. It is evident that the increase of eddy viscosity ratio leads to the decrease of the lift coefficient and increase of the drag coefficient. It is explained by the pressure distributions in figure 7, which shows the significant pressure decrease both on the upper and lower surfaces. Moreover, according to the distributions of turbulence kinetic energy with streamlines in figure 6, it can be seen that the LSB is still visible when the eddy viscosity is equal to 10 and it disappears with the increase of eddy viscosity ratio. With the increase of eddy viscosity ratio from 1 to 10, the location of LSB moves a little upstream and the size shortens, shown in figure 4b, 6a and 7b. As the eddy viscosity further increases, the transition locations both on the upper and lower surfaces move much upstream, which is the reason why

the pressure on both sides change considerably. Based on the relatively small discrepancy of the hydrofoil performance, the eddy viscosity ratio of 10 is employed in the present work.

Table 6 Effect of eddy viscosity ratio on hydrofoil performance

Turbulence intensity (%)-eddy viscosity ratio	Lift coefficient C_l	Error (%)	Drag coefficient C_d
3-1	0.639	7.39	0.00657
3-10	0.585	1.68	0.00630
3-100	0.502	15.63	0.0101
3-1000	0.478	19.66	0.0134
EXP	0.595	--	--

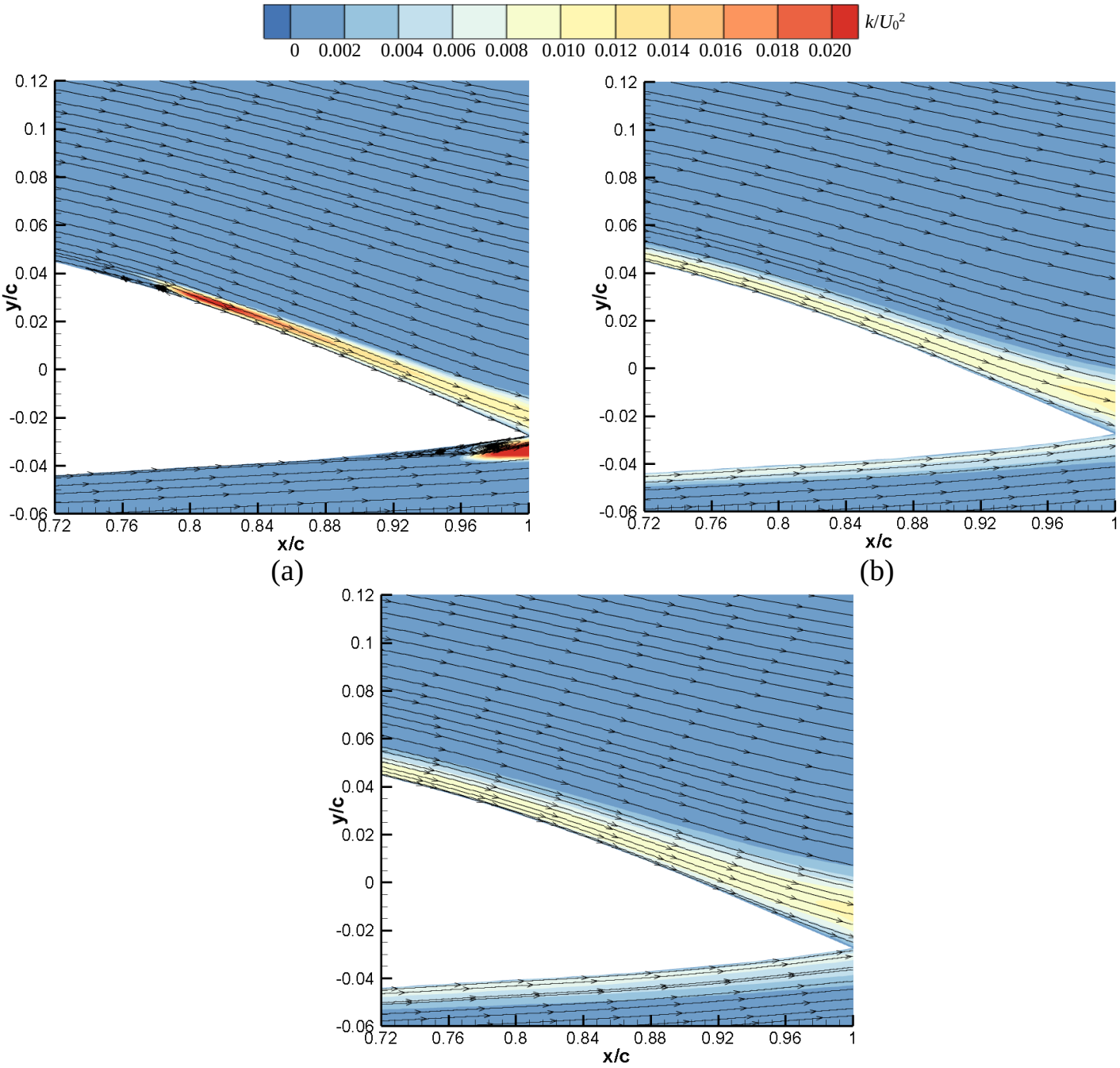

Figure 6 Distributions of turbulence kinetic energy with streamlines at 2°. (a) 3-1; (b) 3-100; (c) 3-1000.

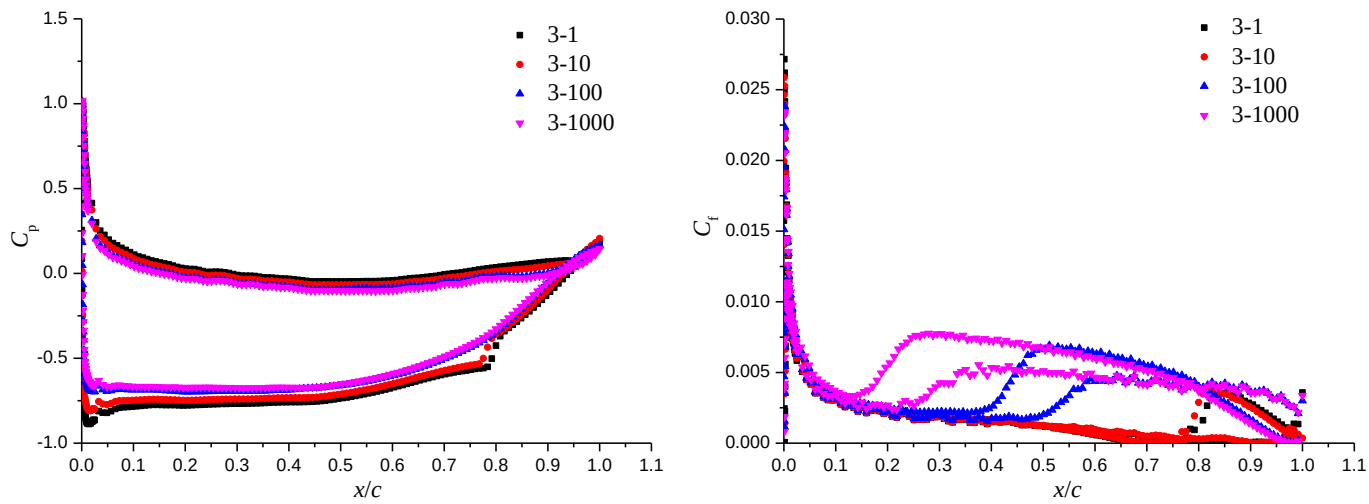

(a) (b)

Figure 7 Distributions of pressure and skin fiction coefficients at 2°. (a) Pressure coefficient; (b) Skin friction coefficient.

4.2 Effect of turbulence model

In this part, the effect of turbulence model on hydrofoil performance is considered, shown by the comparison of results obtained by the SST k-ω model and SST γ-$\widetilde{Re}_{\theta t}$ transition model (SST TM). Figure 8 plots the hydrofoil performance for two turbulence models at different incidences. It is evident that the lift coefficient presents a linear increase before 5°, which shows the same trend with the simulations conducted by Delfin et al. [44] using SST TM. Then, there is a plateau from 5° to 7°. Afterwards, the lift coefficient still increases from 8°. The drag coefficient has a dramatical change as the incidence exceeds 5°, both for the two turbulence models. As the incidence is below 5°, the result of SST TM is better than SST k-ω model, compared with the available experiments [43]. However, the region where the lift has a slow change occurs a little earlier in the experiments. Moreover, there are two main performance transition which is noticeable: the first one is from -3° to -1° and the other one is from 5° to 8°, which will be discussed later.

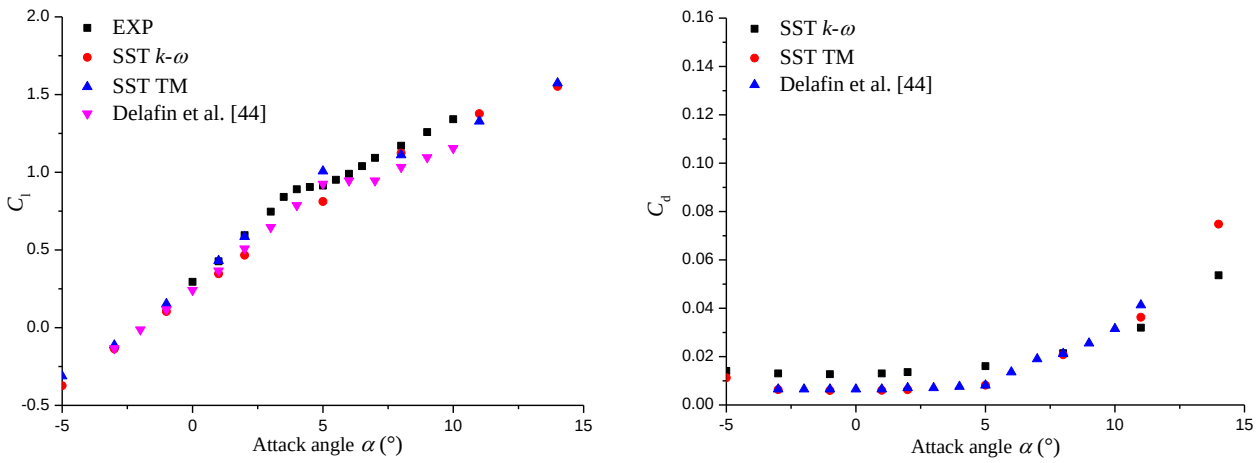

(a) (b)

Figure 8 Hydrofoil performance for two turbulence models. (a) Lift coefficient; (b) Drag coefficient.

Figure 9 shows the mean velocity profiles at different locations for the two turbulence models at 2°and the results are compared with the available experiments [42]. U is the velocity component in the streamwise and U_{ext} is the velocity at the thickness of the boundary layer. At x/c=0.60, the flow is in the laminar boundary layer which still attaches on the foil surface. Then, at x/c=0.72, it is located in the vicinity of the separation point, shown by the small portion of the negative velocity very close to the wall. Furthermore, a bulk of the reverse flow is detected inside the LSB at x/c=0.76, shown by figure 5c. When the flows come across the LSB, it would reattach on the foil surface at x/c=0.84. As it develops after the reattachment at x/c=0.90, the turbulent boundary layer emerges and the inside vortex filaments would shed into the wakes. In general, the prediction of the velocity profiles obtained by SST TM is much better than SST k-ω model, even inside the LSB and in the turbulent boundary layer, where the reverse flow and vortical flow dominant respectively.

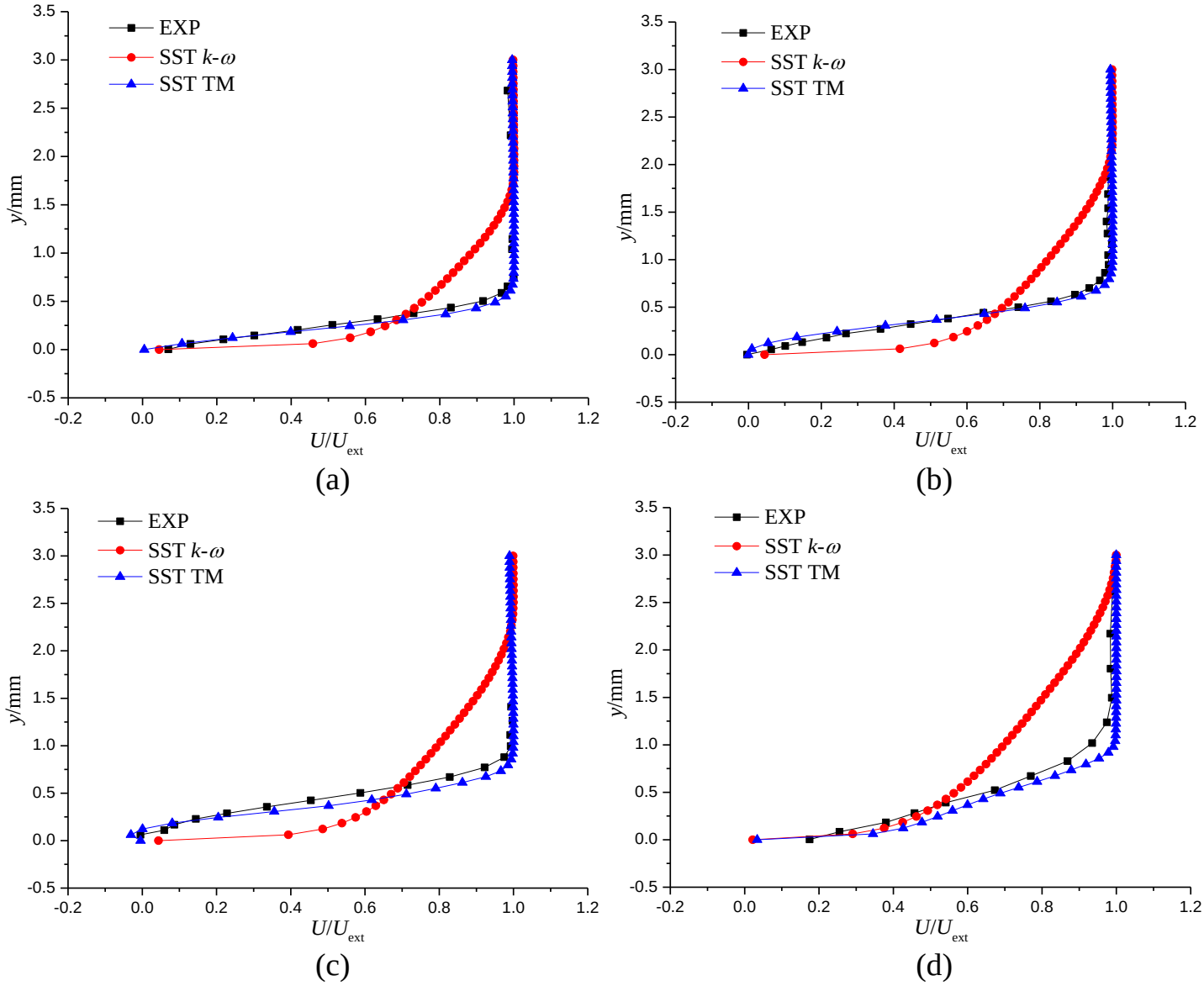

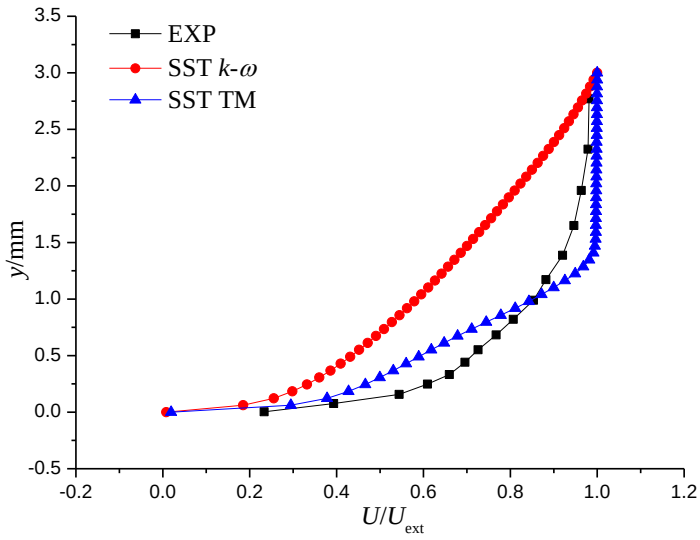

(e)

Figure 9 Mean velocity profiles at different locations for 2°. (a) x/c=0.60; (b) x/c=0.72; (c) x/c=0.76; (d) x/c=0.84; (e) x/c=0.90.

In figure 10, four attack angles are adopted to explain the performance transition by the distributions of turbulence kinetic energy and pressure coefficient. From -3° to -1°, the transition location moves upstream slightly and the magnitude of turbulence kinetic energy becomes smaller. However, the pressure difference shown in figure 10e for two incidences are quite different. Compared with -3°, only a small part of the hydrofoil at -1° is occupied by the negative pressure difference, which is mainly near the leading edge. However, when it comes to the second performance transition, it is observed that the transition location from the middle chord at 5° suddenly moves to the leading edge at 8°, totally changing the turbulence kinetic energy and pressure distributions on the suction surface. Therefore, it concludes that the former performance transition from -3° to -1° is ascribed to the shift of zero pressure difference point while the LSB location movement from the middle chord to the leading edge from 5° to 8° should be responsible for the pressure distribution on the suction side.

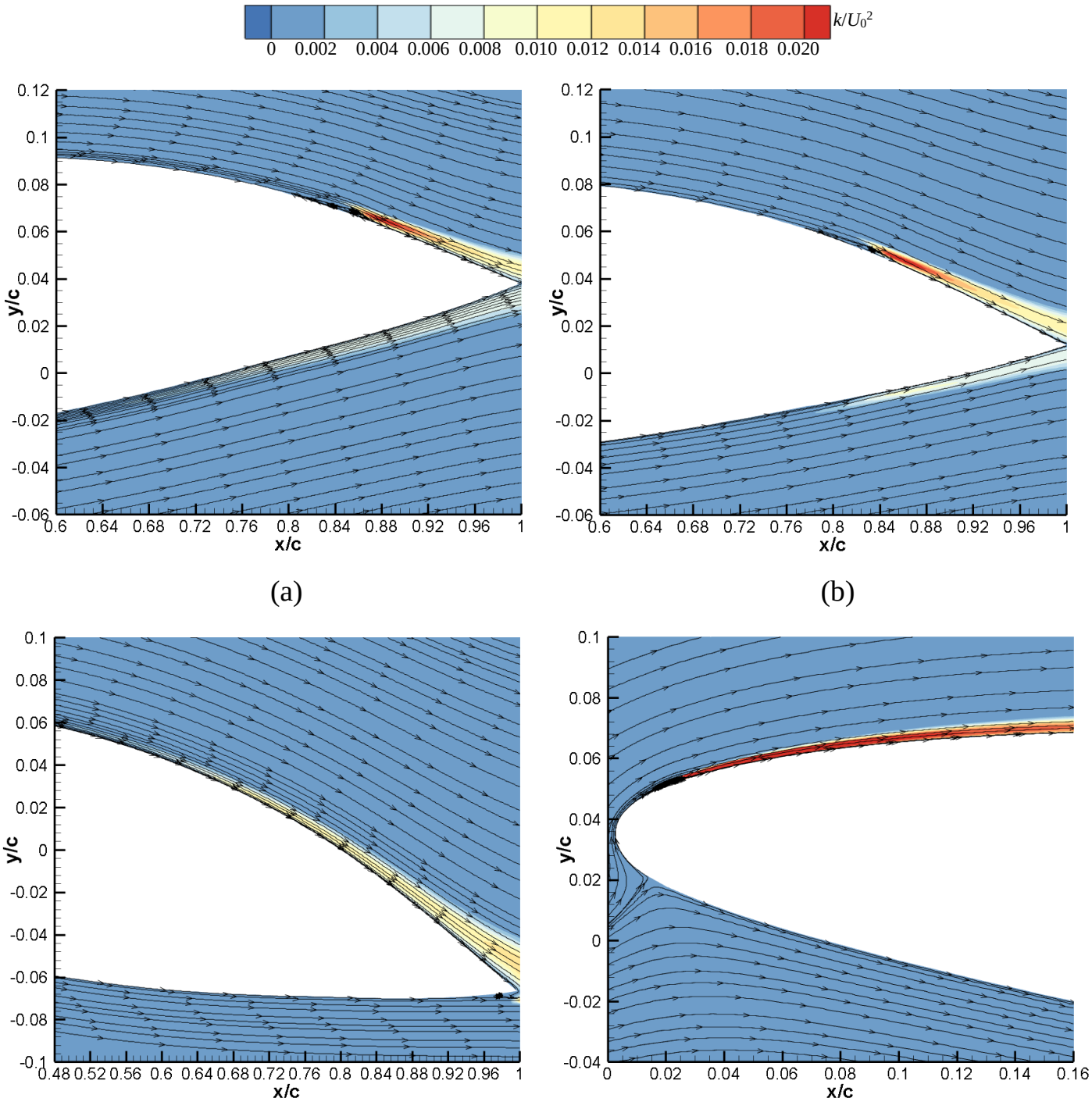
k/U0²
0 0.002 0.004 0.006 0.008 0.010 0.012 0.014 0.016 0.018 0.020
y/c
x/c
(a)
(b)
(c)
(d)

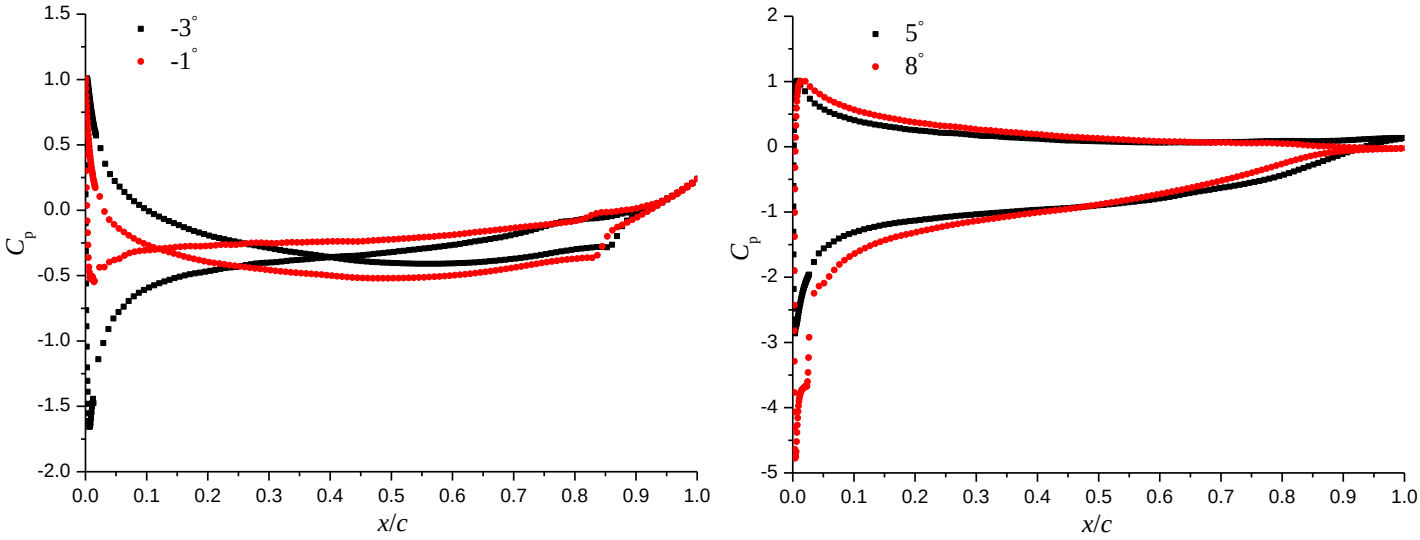

(e) (f)

Figure 10 Distributions of turbulence kinetic energy with the streamlines and pressure coefficient for SST TM. (a) -3°; (b) -1°; (c) 5°; (d) 8°; (e) -3° and -1°; (f) 5° and 8°.

The distributions of turbulence kinetic energy for the two turbulence models are presented at different incidences in figure 11, to clarify the difference in flow morphology near the solid wall. At -5°, the transition on the pressure side is located near the leading edge. Then, at 2°, it moves downstream and occurs near the trailing edge (TE) of the suction side. As the incidence increases to 11°, the transition appears near the leading edge of the suction surface. Moreover, it can be seen that the larger value of turbulence kinetic energy can be resolved by the transition model compared with SST *k*-*ω* model, which can be associated with the modified *k* equation in the transition model. In addition, the SST *k*-*ω* model can only resolve the fully turbulent flows while the transition model can predict the transition location obviously induced by the LSB.

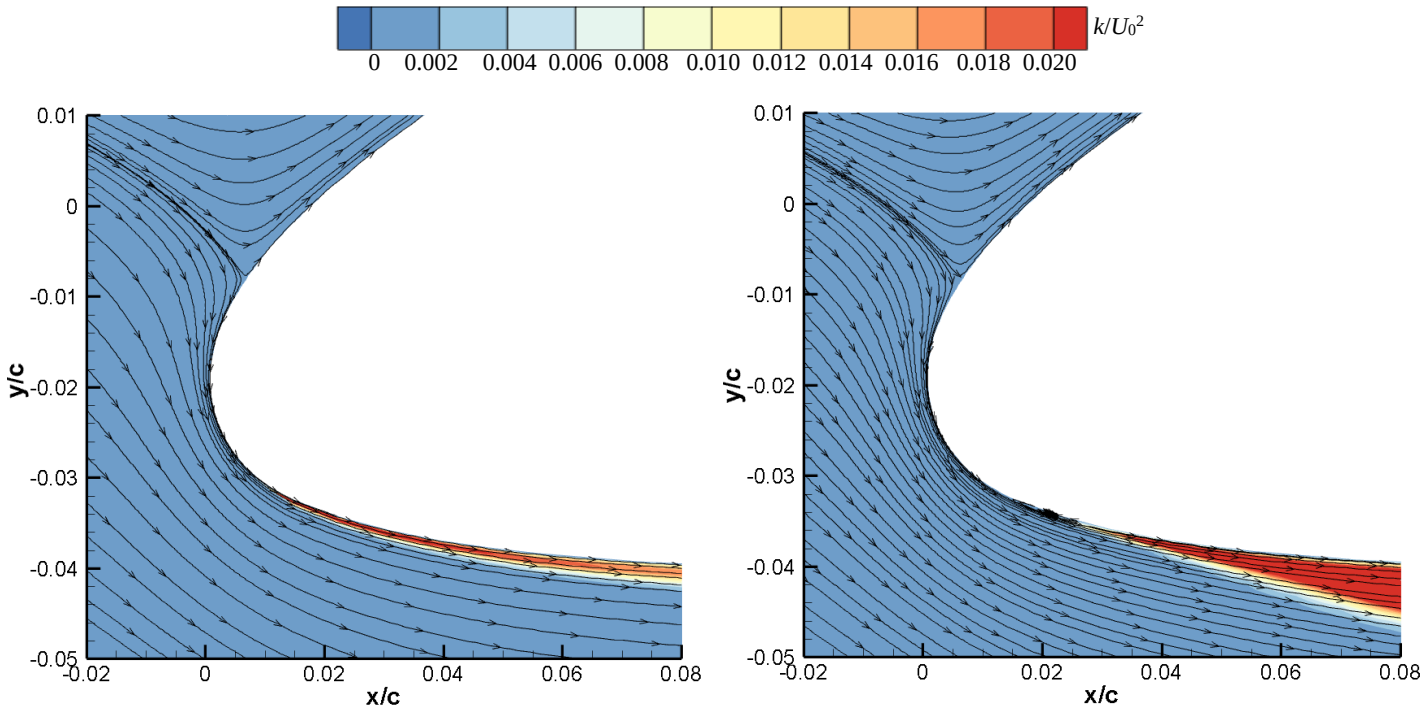

(a) (b)

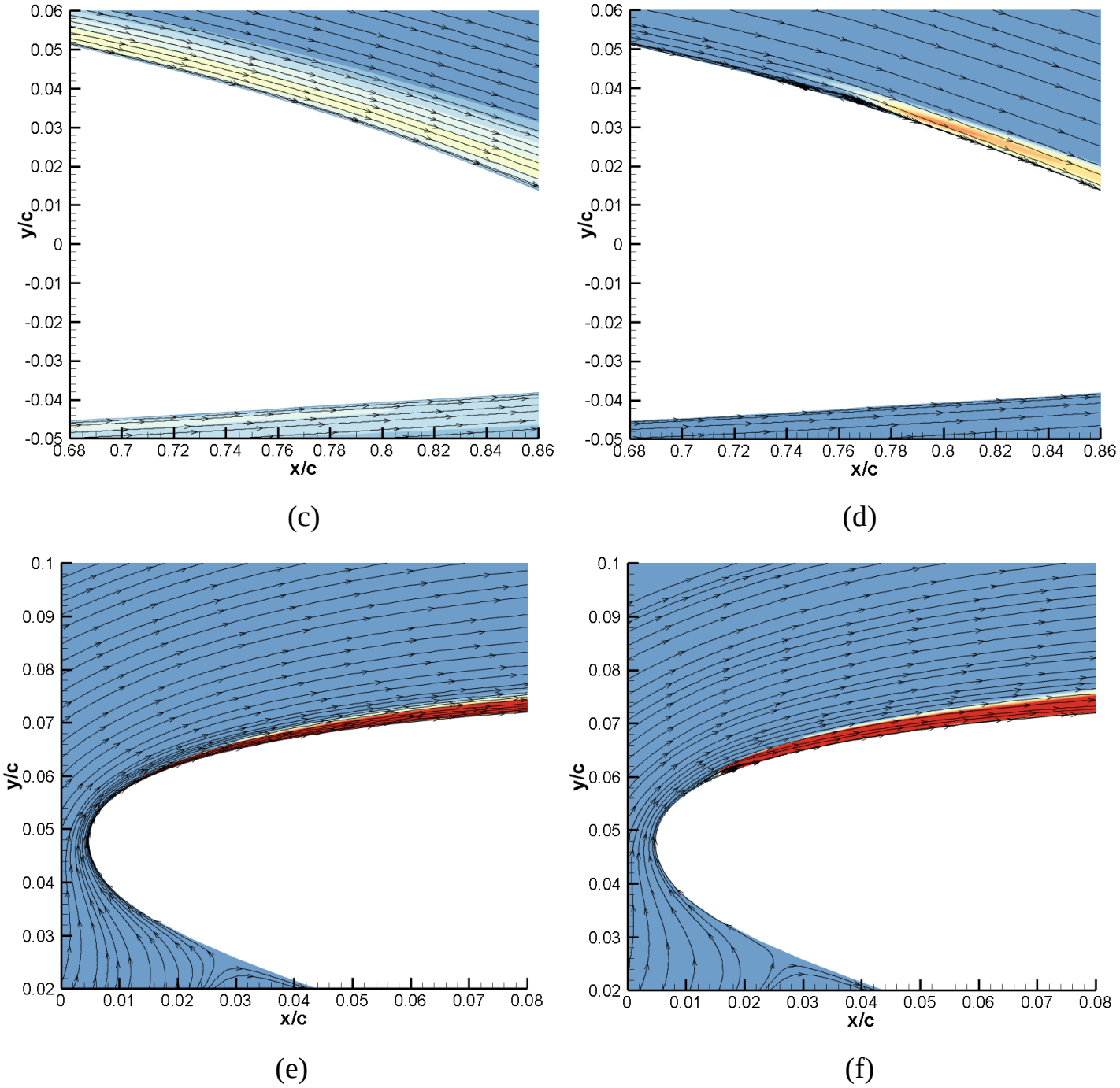

Figure 11 Distributions of turbulence kinetic energy with the streamlines. (a) SST *k-ω* -5°; (b) SST TM -5°; (c) SST *k-ω* 2°; (d) SST TM 2°; (e) SST *k-ω* 11°; (f) SST TM 11°.

Figure 12 characterizes the separation (S), transition (T) and reattachment (R) points at different incidences both on the suction and pressure sides. The distribution of intermittency can be used to determine the separation, transition and reattachment locations clearly, shown by the figure 12a at 8°. The value of intermittency equal to 0 represents the laminar flow while the turbulent flow can be indicated by the value of 1. According to the figure 12b, it can be seen that the transition location will move downstream on the pressure side while it moves upstream along the suction side, as the incidence increases. When the attack angle is equal to -5° or exceeds 5°, the transition on one surface is far away from the other surface, indicating that the boundary layer is quite asymmetrical. For a specific example, at 8°, the flow on the pressure

side near the trailing edge is not reattached, forming an open recirculation region that can be the source of the unstable flows.

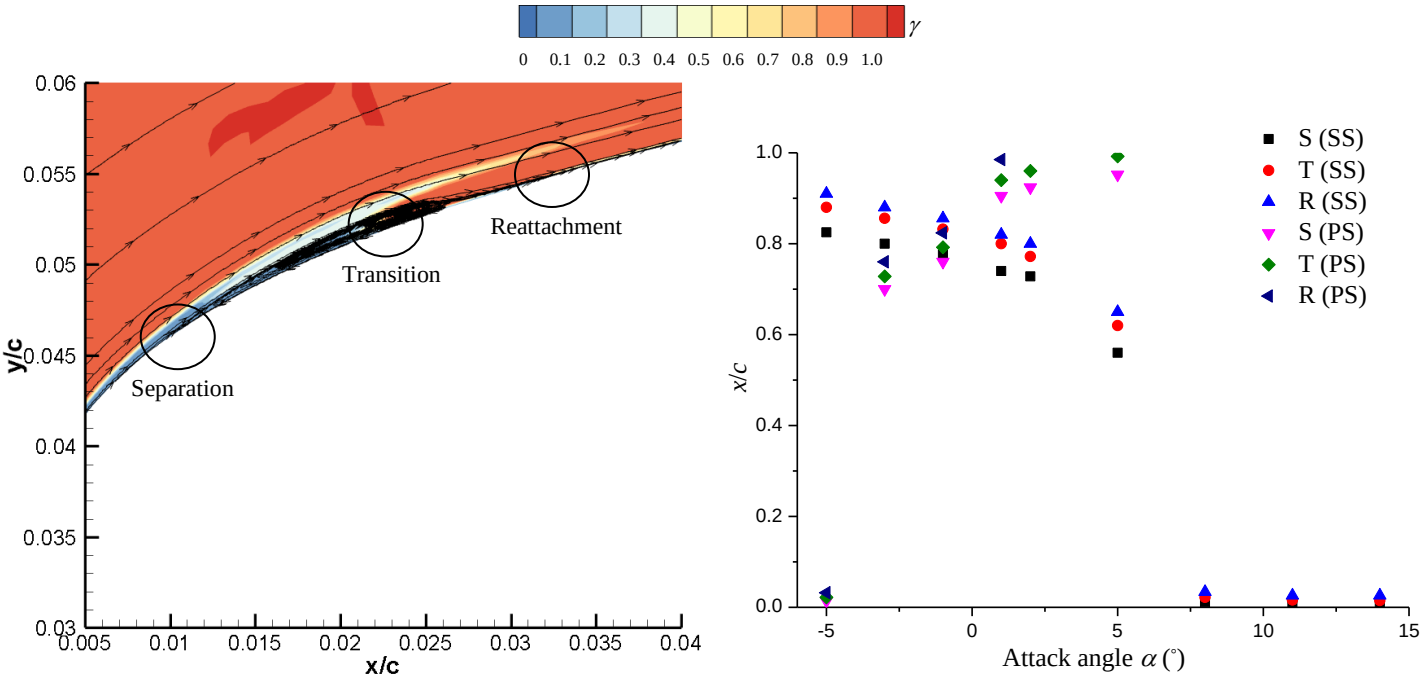

(a) (b)

Figure 12 Transition locations at different incidences. (a) Intermittency at 8°; (b) Separation, transition and reattachment points on the suction and pressure sides.

4.3 Effect of Reynolds number on reverse flow

In this section, the transitional flow around the reversed hydrofoil and the Reynolds number effect will be discussed in detail. In figure 13, the reversed hydrofoil performance for Reynolds number 7.5×10^4, 1.5×10^5, 4.5×10^5 and 7.5×10^5 are plotted and the results are compared with the forward configuration at 7.5×10^5. When the incidence is below 2°, the lift coefficient of reversed hydrofoil is almost the same with that for forward hydrofoil and it nearly has the linear increase. However, it increases slowly after 2° and the corresponding drag coefficient increases dramatically, resulting in the large performance difference compared with the forward hydrofoil. This phenomenon is ascribed to the change of transition point from 2° to 5° for reversed hydrofoil and from 5° and 8° (actually at 6°) for forward hydrofoil. Moreover, the reversed hydrofoil performance increases with the Reynolds number but the difference is not too much. The detailed near-wall flow structures will be shown to clarify the effect of transition on the reversed hydrofoil performance at different incidences.

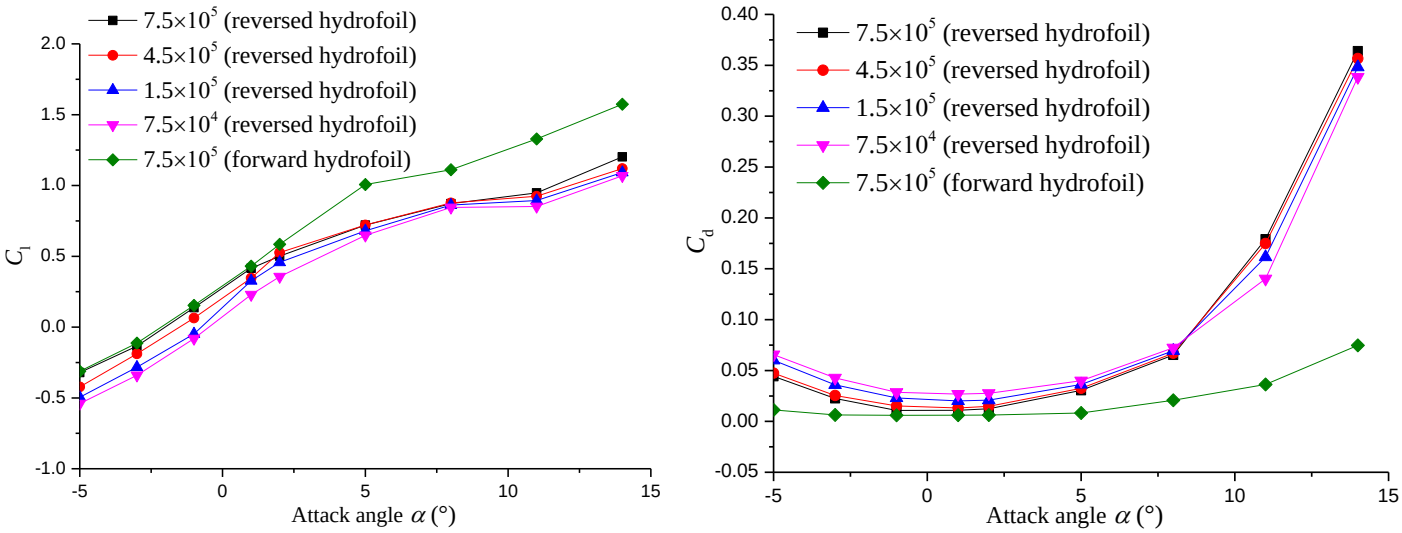

(a) (b)

Figure 13 Forward and reversed hydrofoil performance for different Reynolds number. (a) Lift coefficient; (b) Drag coefficient.

The dynamics of transitional and separation flows over the reversed hydrofoils at Re=7.5×10^5 are presented in figure 14, using the distributions of turbulence kinetic energy coupled with the streamlines. At -5°, near the leading edge where the flow separation-induced transition occurs, a large-scale (RDV) is observed evidently on the lower surface, and the flow detaches from the sharp leading edge and then it reattaches at about x/c=0.35. Meanwhile, on the upper surface, the transition emerging at about x/c=0.93 can also be captured. The flow from two sides interacts with each other and a vortex structure appears near the trailing edge. According to the location of the trailing edge vortex, it concludes that it is earlier as the flow on the upper surface reaches to the trailing edge. Then, at -1°, the transition on both sides seems symmetrical and a pair of vortex structures form near the trailing edge. When the incidence increases to 2°, the transition on the upper side moves upstream while it is more downstream on the lower surface. Simultaneously, the symmetrical vortex pair generated at -1° becomes quasi-symmetrical and it moves to the upper surface gradually. Moreover, at 5° shown in figure 14e, the transition induced by RDV is located at the leading edge on the upper surface, which happens in advance compared with the forward hydrofoil. At the same time, the quasi-symmetrical vortex pair integrates into a single structure and it moves upstream along the upper surface at 8° and 11°. In figure 14g and 14h, the transition location moves more upstream, which approximately approaches to the sharp leading edge as the incidence still increases. The RDV becomes larger with the attack angle, shown by the height and length of this large-scale structure. By the comparison, it concludes that the separation-induced RDV over the reversed foil is much larger than that on the forward hydrofoil and the flow near the trailing edge is also quite different.

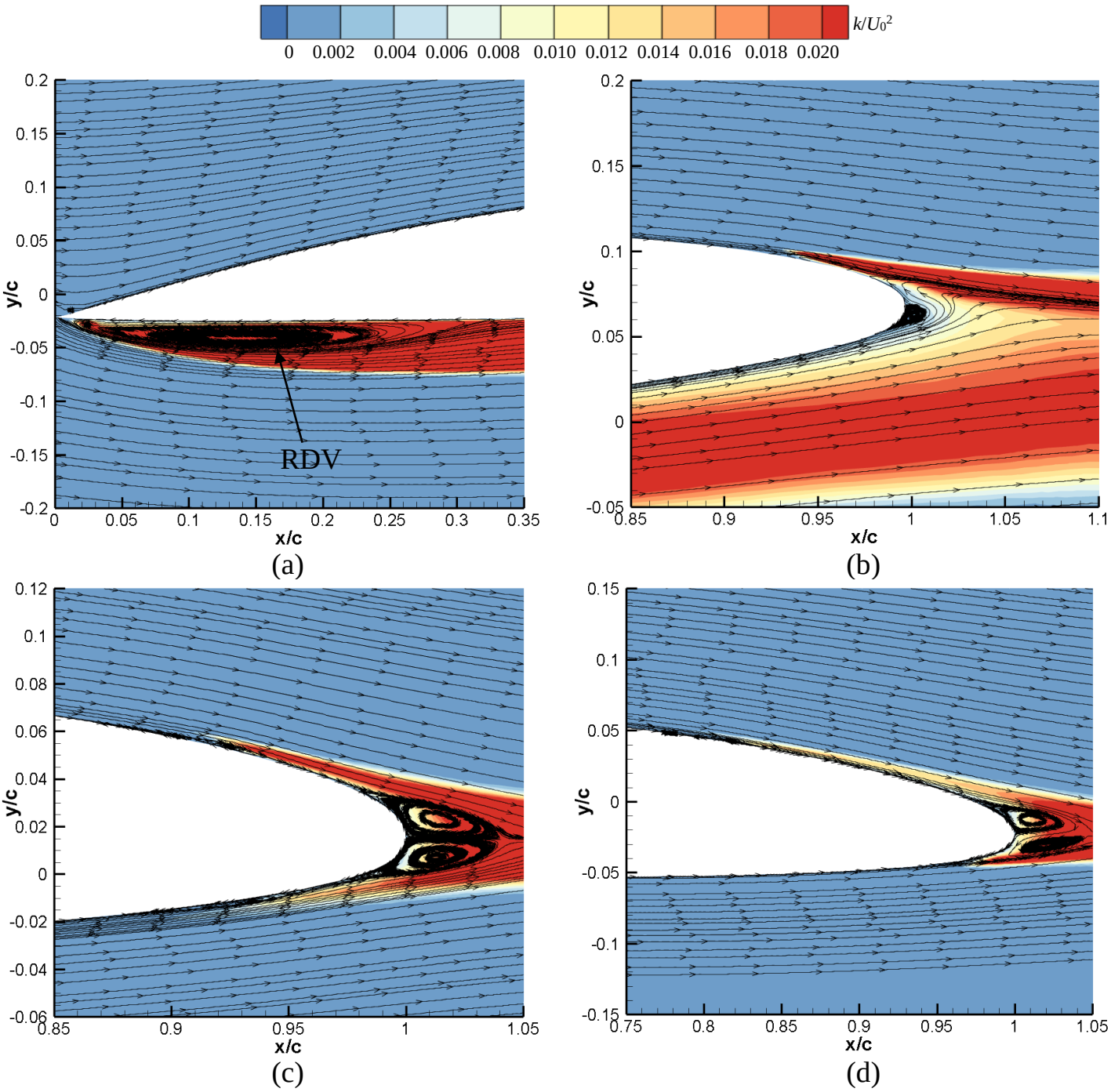
k/U0²
0 0.002 0.004 0.006 0.008 0.010 0.012 0.014 0.016 0.018 0.020
RDV
y/c
x/c
(a)
(b)
(c)
(d)

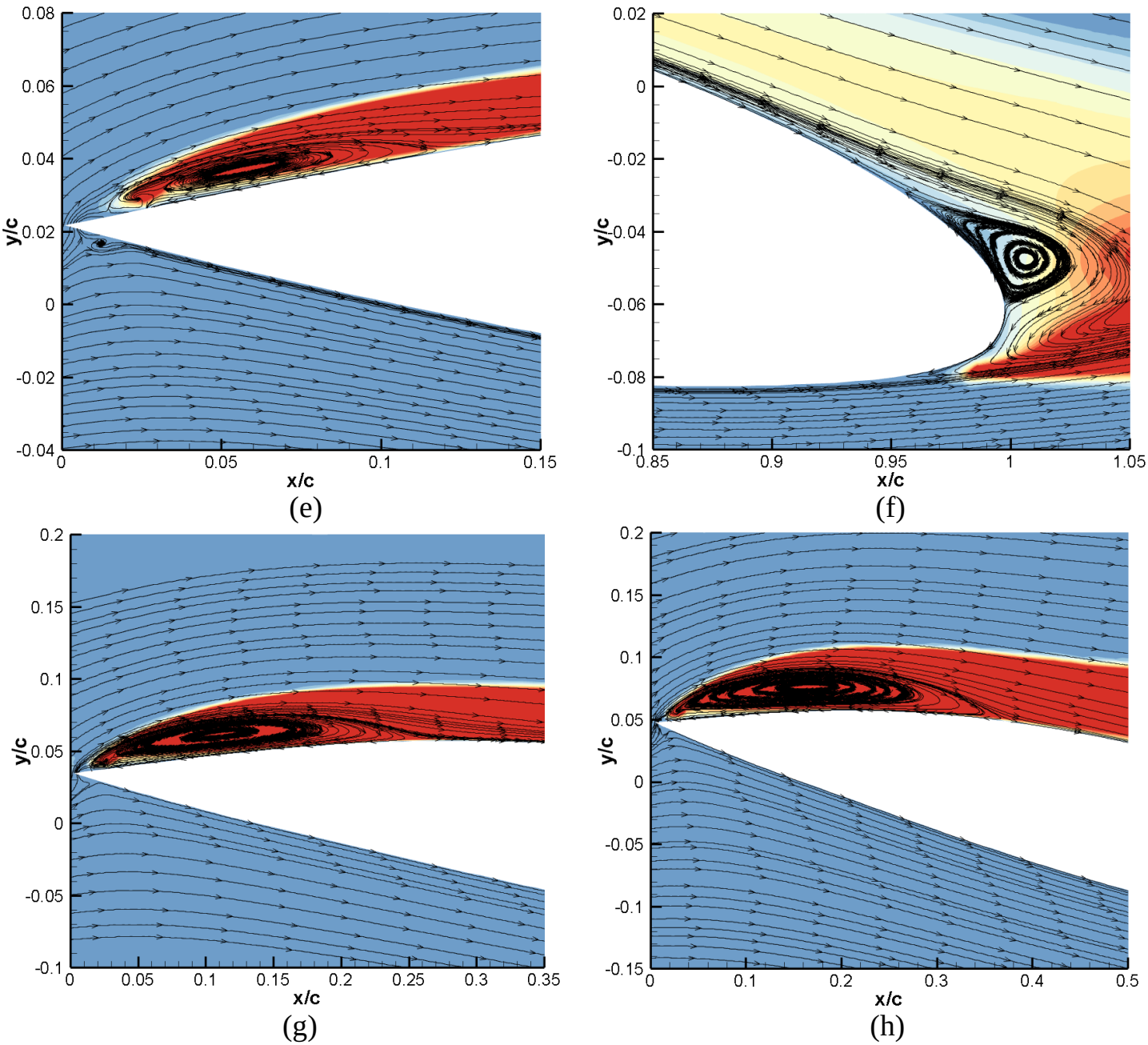

Figure 14 Transition over the reversed hydrofoil at different incidences. (a) Leading edge at -5°; (b) Trailing edge at -5°; (c) Trailing edge at -1°; (d) Trailing edge at 2°; (e) Leading edge at 5°; (f) Trailing edge at 5°; (g) Leading edge at 8°; (h) Leading edge at 11°.

Figure 15 plots the distributions of pressure coefficients on the foil surface at various incidences, to illustrate the transition effect on the hydrodynamic performance at Re=7.5×10^5. At -5°, on the lower surface, the transition is located at the leading edge and the pressure decreases in the region of RDV. Near the trailing edge of the suction side, the transition can also be observed. At this incidence, large part of the leading edge is occupied by the negative pressure difference, resulting in the negative performance. However, at -1°, the region of the negative pressure difference near the leading edge becomes small and the performance becomes positive, shown in figure 13a. The transition both on the two sides are evident, but it is more upstream on the suction side. As the incidence increases to 2°, the transition location moves upstream and it nearly approaches to x/c=0.80. Then, at 5°, 8° and 11°, the transition is always

near the leading edge of the upper surface and the pressure decrease region becomes larger when the incidence increases, which is induced by the expansion of RDV.

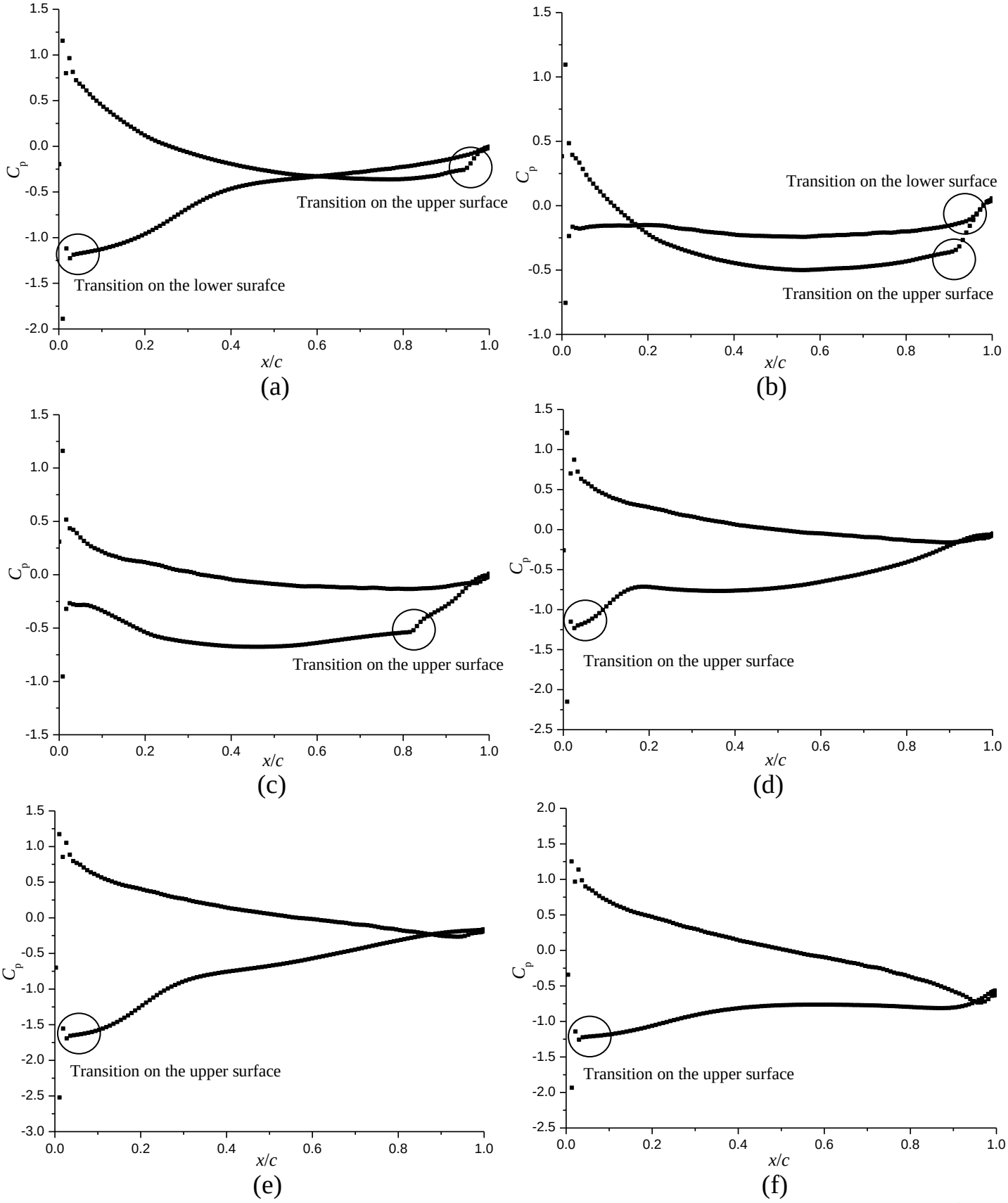

Figure 15 Pressure distributions over the reversed hydrofoil at difference incidences. (a) -5°; (b) -1°; (c) 2°; (d) 5°; (e) 8°; (f) 11°.

The separation, transition and reattachment locations both on lower and upper surfaces of the reversed hydrofoil are mapped in figure 16, to show how it moves with the change of the incidence. It can be seen that with the increase of the incidence, the transition on the lower surface will move towards the trailing edge while it moves from the trailing edge to the leading edge over the upper surface. When the attack angle is lower than -3° and larger than 5°, the transition on one surface is far away from the other side, leading to the extremely asymmetrical boundary layer. Simultaneously, the flow near the trailing edge is not reattached and it mixes with the separation flows. At larger incidence, for example, 14°, there is no reattachment on the upper surface even the transition occurs near the leading edge and a large-scale vortex structure is generated moving downstream.

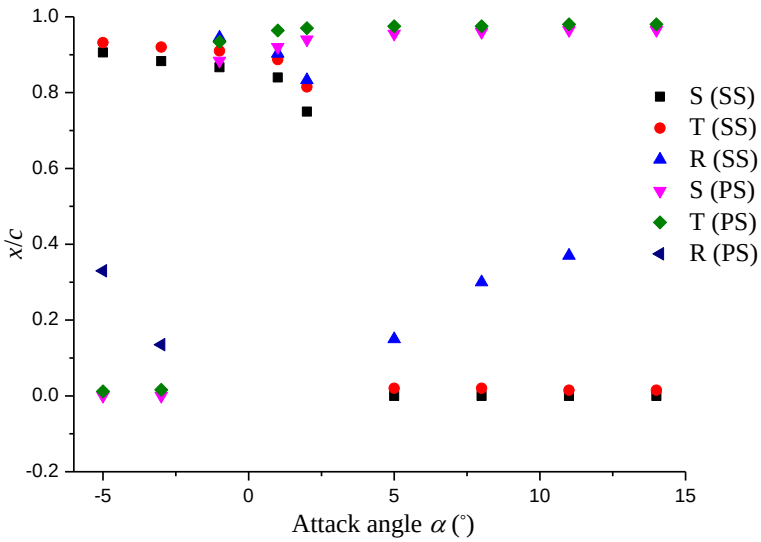

Figure 16 Separation, transition and reattachment points for different incidences.

In figure 17, 18 and 19, the effect of Reynolds number on the transition and hydrodynamic performance is analyzed, using the turbulence kinetic energy contours coupled with streamlines, and the pressure coefficient distributions. At negative incidence of -5°, the large-structure RDV is near the leading edge over the upper surface. As the Reynold number decreases, the magnitude of turbulence kinetic energy also decreases due to the low inflow velocity. The pressure coefficient distributions show that the negative pressure difference becomes larger as the Reynolds number decreases, resulting in the larger negative performance. At 1° in figure 18, the transition mainly occurs near the trailing edge where there is a pair of the vortex structures. When decreasing the Reynolds number, the transition region gradually mixes with the recirculation region of the vortex pair, resulting in the thick boundary layer there. Simultaneously, it is observed that the transition on the upper side moves downstream slightly with the decrease of the Reynolds number from 7.5×10^5 to 4.5×10^5, which is also presented by the pressure distribution in figure 18f. Then, at 5°, the transition moves upstream and it is located near the leading edge of the suction side. At the same time, the vortex pair near the trailing edge becomes asymmetrical and it moves towards the upper surface, bringing about the decrease of the pressure, which is more evident as the Reynolds number increases. In general, it concludes that the Reynolds number has an impact on the distributions of turbulence kinetic energy for all the tested cases and flow morphology at 1° near the trailing edge.

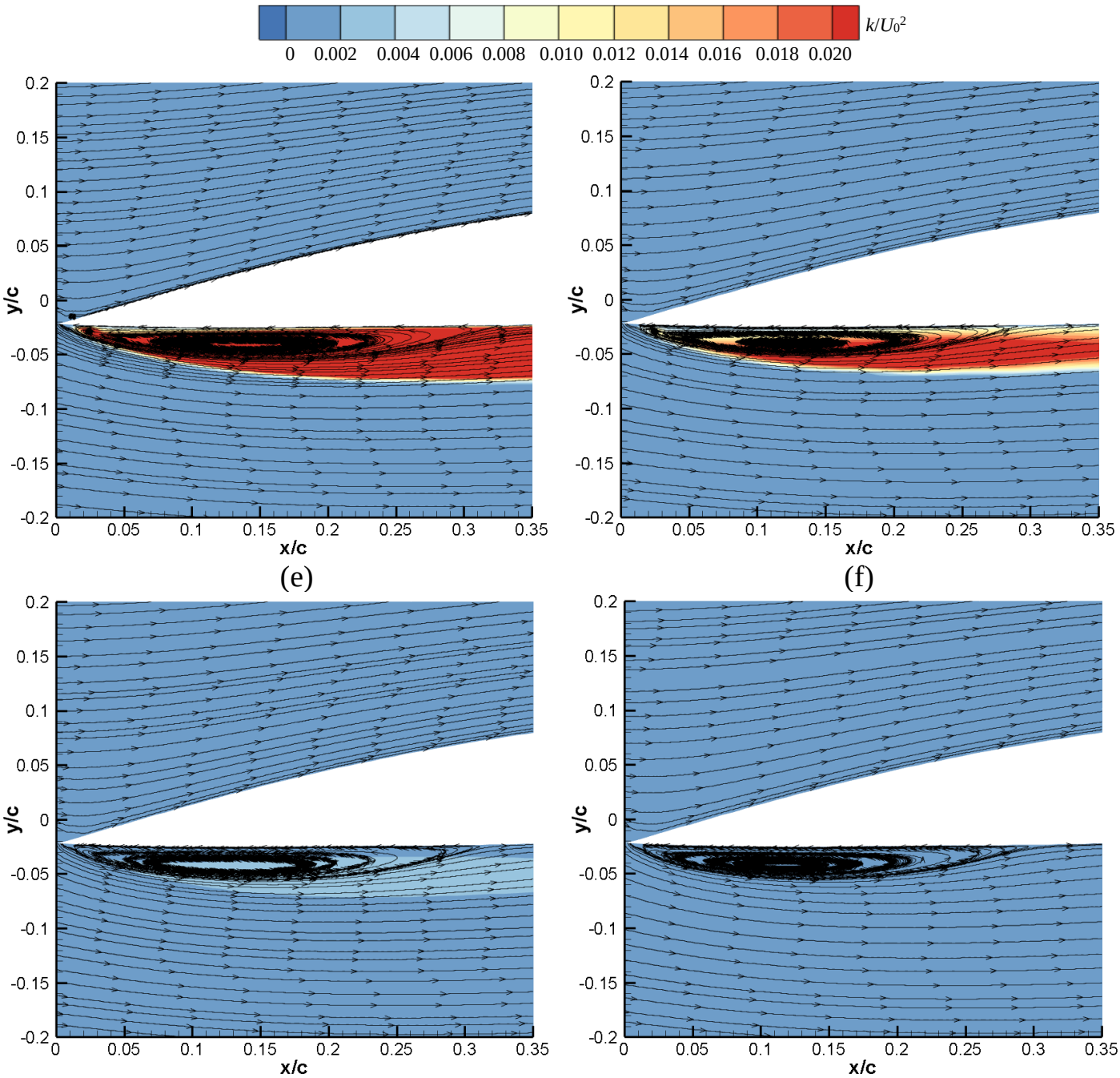
k/U0²
0 0.002 0.004 0.006 0.008 0.010 0.012 0.014 0.016 0.018 0.020
y/c
x/c
(e)
(f)
(c)
(d)

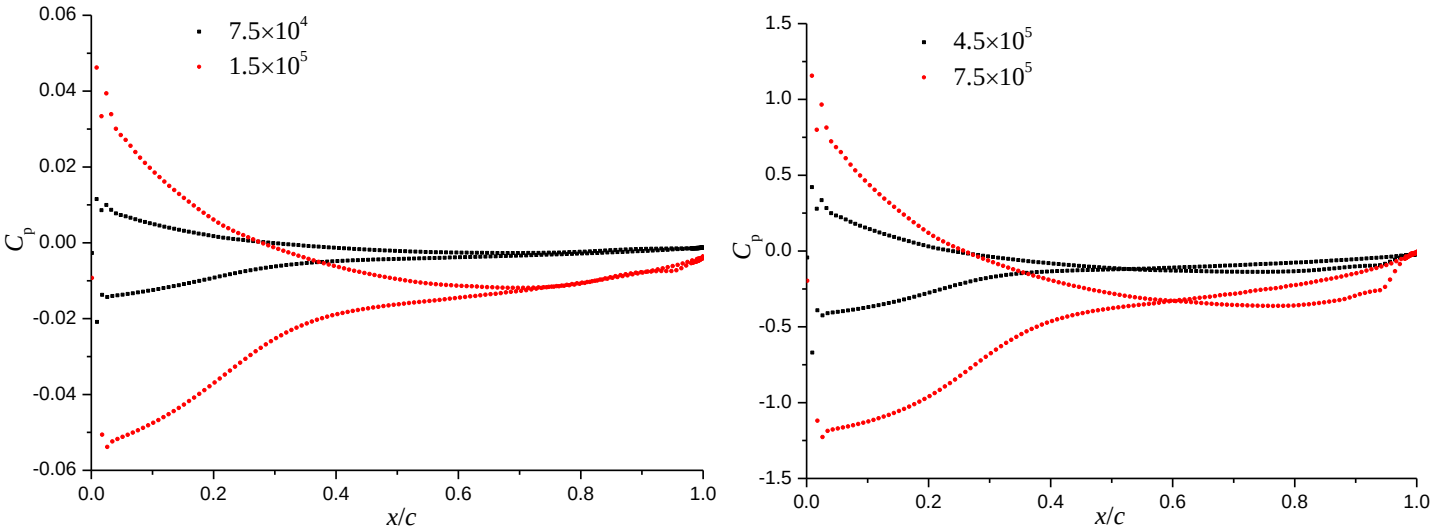

(e) (f)

Figure 17 Distributions of turbulence kinetic energy and pressure coefficient at -5° for various Reynolds numbers. (a) 7.5×10^5; (b) 4.5×10^5; (c) 1.5×10^5; (d) 7.5×10^4; (e) 7.5×10^4 and 1.5×10^5; (f) 4.5×10^5 and 7.5×10^5.

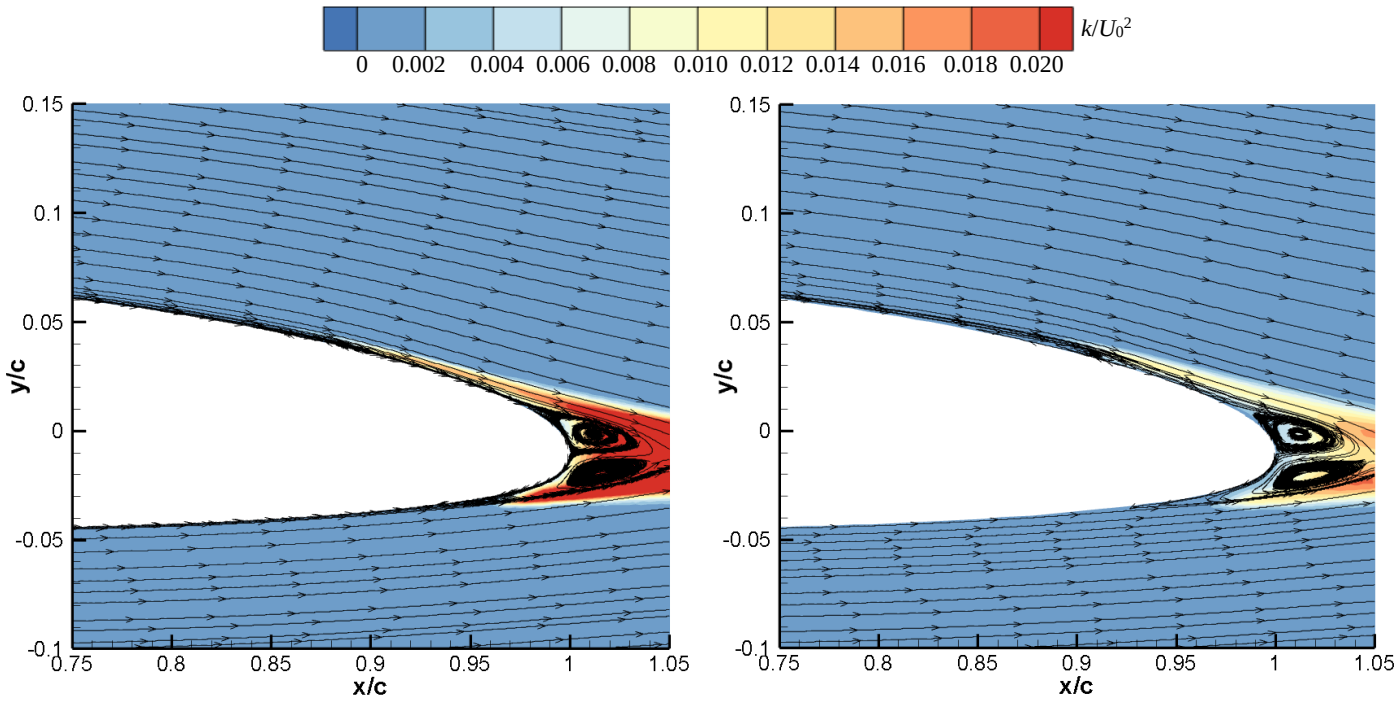

(a) (b)

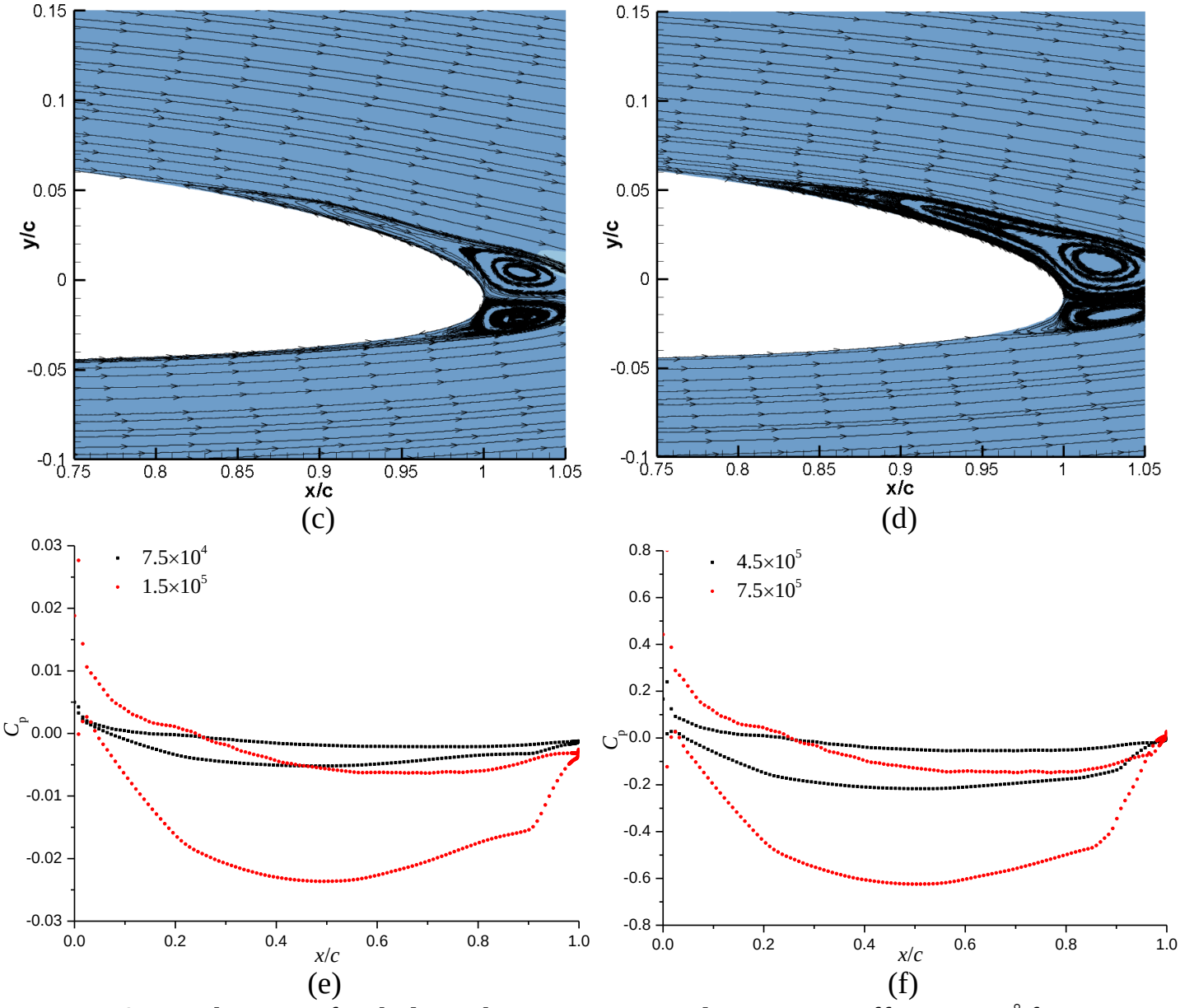

Figure 18 Distributions of turbulence kinetic energy and pressure coefficient at 1° for various Reynolds numbers. (a) 7.5×10^5; (b) 4.5×10^5; (c) 1.5×10^5; (d) 7.5×10^4; (e) 7.5×10^4 and 1.5×10^5; (f) 4.5×10^5 and 7.5×10^5.

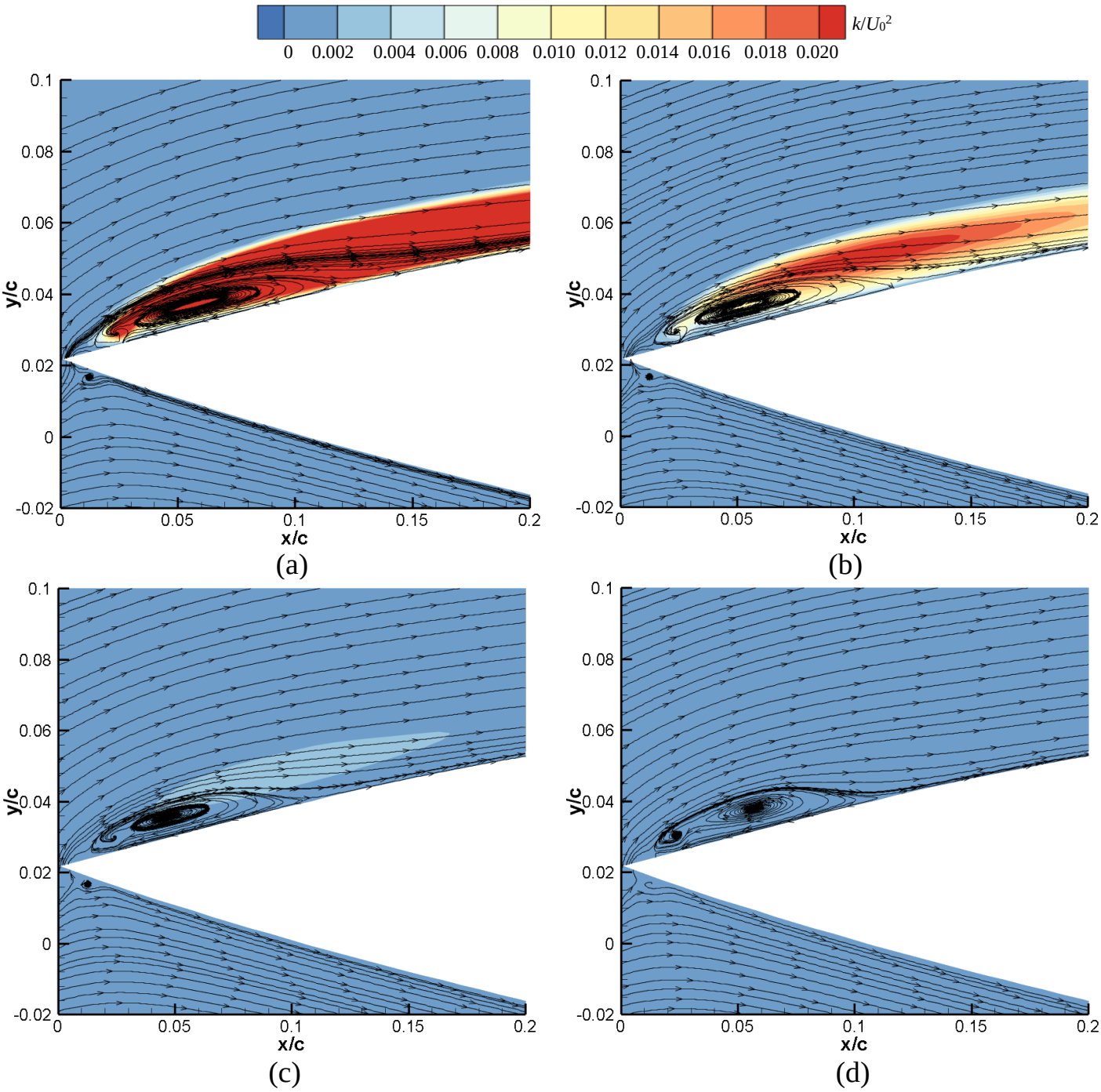
k/U0²
0 0.002 0.004 0.006 0.008 0.010 0.012 0.014 0.016 0.018 0.020
y/c
x/c
(a)
(b)
(c)
(d)

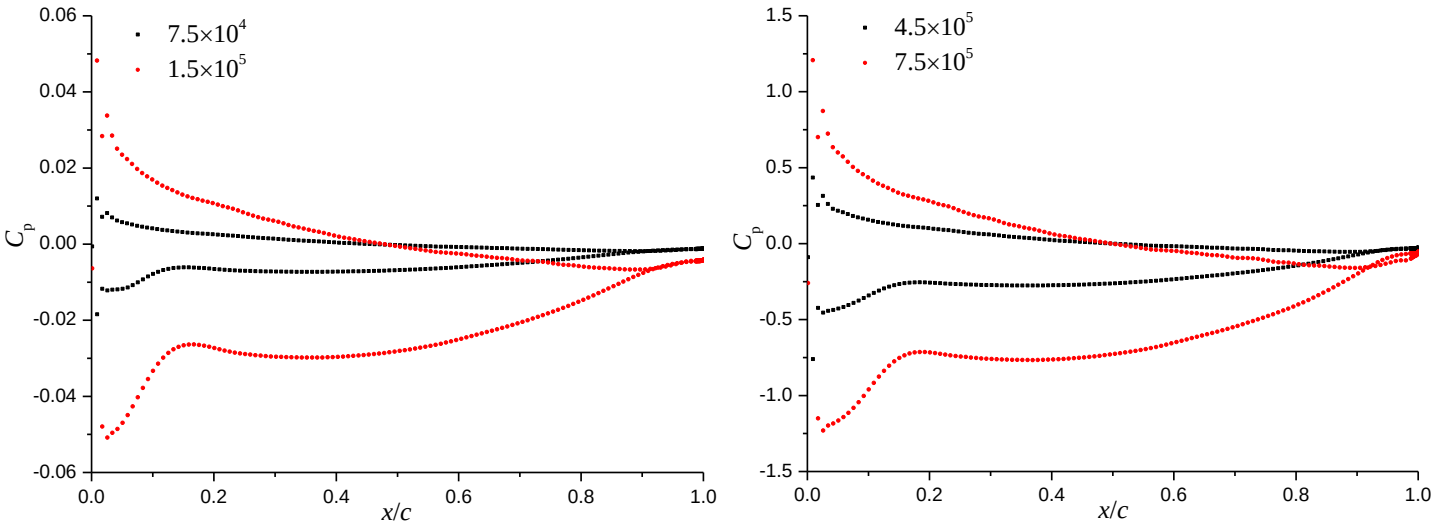

(e) (f)

Figure 19 Distributions of turbulence kinetic energy and pressure coefficient at 5° for various Reynolds numbers. (a) 7.5×10^5; (b) 4.5×10^5; (c) 1.5×10^5; (d) 7.5×10^4; (e) 7.5×10^4 and 1.5×10^5; (f) 4.5×10^5 and 7.5×10^5.

To illustrate the effect of the Reynolds number on the dynamics of the flow separation and reattachment, the mean velocity profiles at different locations are plotted in figure 20, 21 and 22. At -5°, it is in the region of large-scale RDV at x/c=0.05, shown by the negative velocity very close to the wall. Meanwhile, the reverse flow induced by RDV is more intensive with the decrease of the Reynolds number. Then, the negative velocity for 7.5×10^5 becomes large gradually and it has the largest value at x/c=0.3, which indicates that the flow separation point is delayed for 7.5×10^5 and the reattachment point is also more downstream compared with that for other three Reynolds numbers. In addition, it is observed that the thickness of boundary layer decreases as the Reynolds number increases, but at 4.5×10^5, the boundary layer thickness is thinnest. Furthermore, at this Reynolds number, the flow is reattached at x/c=0.3 represented by the positive velocity near the solid wall, which shows that the length of RDV is smallest. When it comes to the incidence of 2° in figure 21, there is no flow separation at x/c=0.7 and it is still the laminar boundary layer. However, the flow separation appears at x/c=0.8 for both four Reynolds numbers, but it is more evident for 1.5×10^5 and 7.5×10^4. Afterwards, the flow is reattached at x/c=0.85 for 7.5×10^5 and at x/c=0.9 for 4.5×10^5. The strong reverse flows emerge after x/c=0.8 for 7.5×10^4 and 1.5×10^5, induced by the mixture of the transition region with the recirculation area near the trailing edge shown in figure 18, which is more apparent for the low Reynolds number. When the transition is located near the leading edge at 8° in figure 22, the trend is more similar with that at -5° except for Reynolds number 4.5×10^5. With the increase of the Reynolds number, the flow separation is delayed near the leading edge while the reattachment point is located more downstream. However, the change of boundary layer thickness has the different trend inside the recirculation region near the leading edge at -5° and 8° for various Reynolds numbers. Therefore, it concludes that the Reynolds number can influence the near-wall flows at various incidences, in terms of the flow morphology and the transition for the reversed hydrofoil.

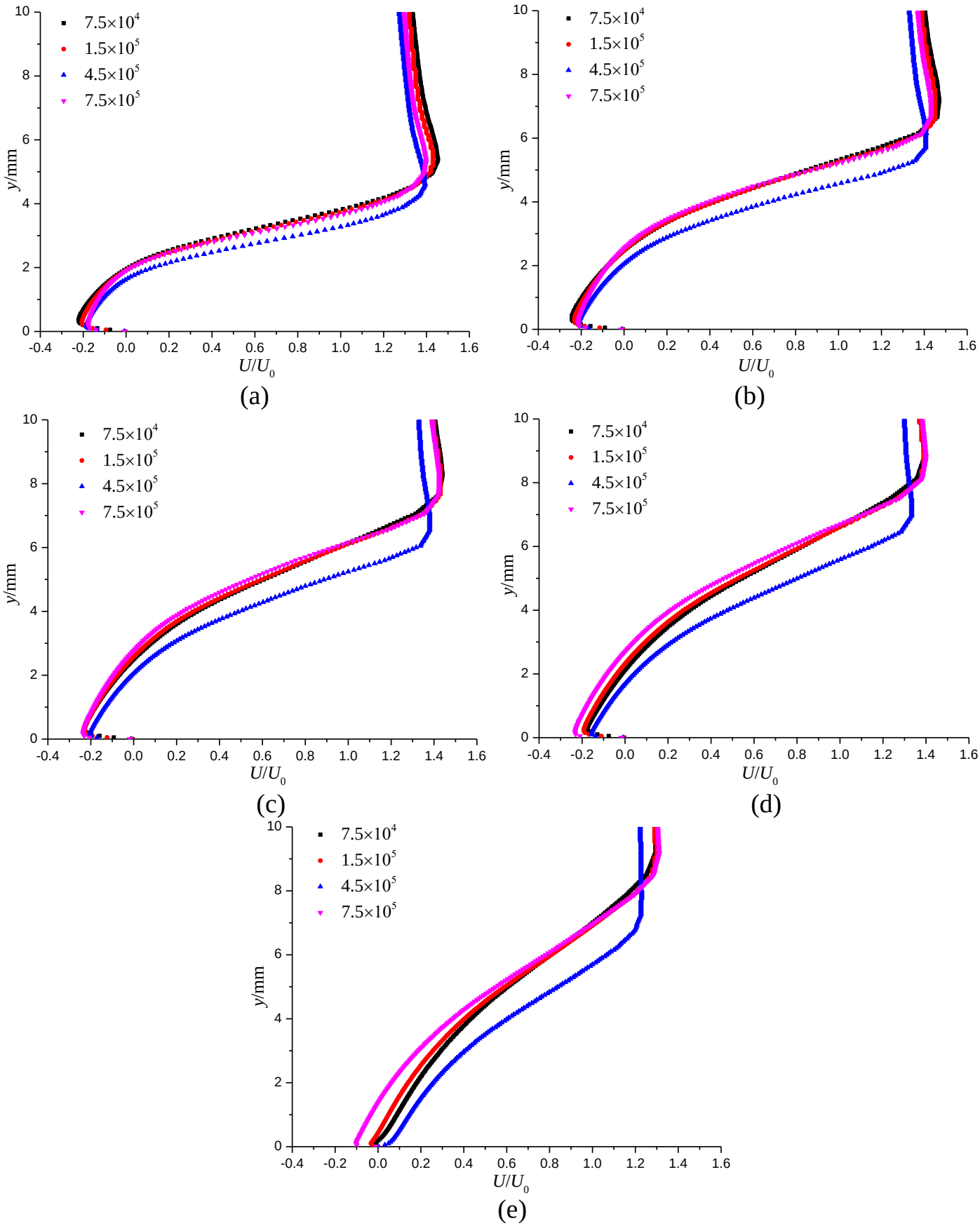

Figure 20 Mean velocity profiles at -5° for various Reynolds numbers. (a) x/c=0.05; (b) x/c=0.1; (c) x/c=0.15; (d) x/c=0.2; (e) x/c=0.3.

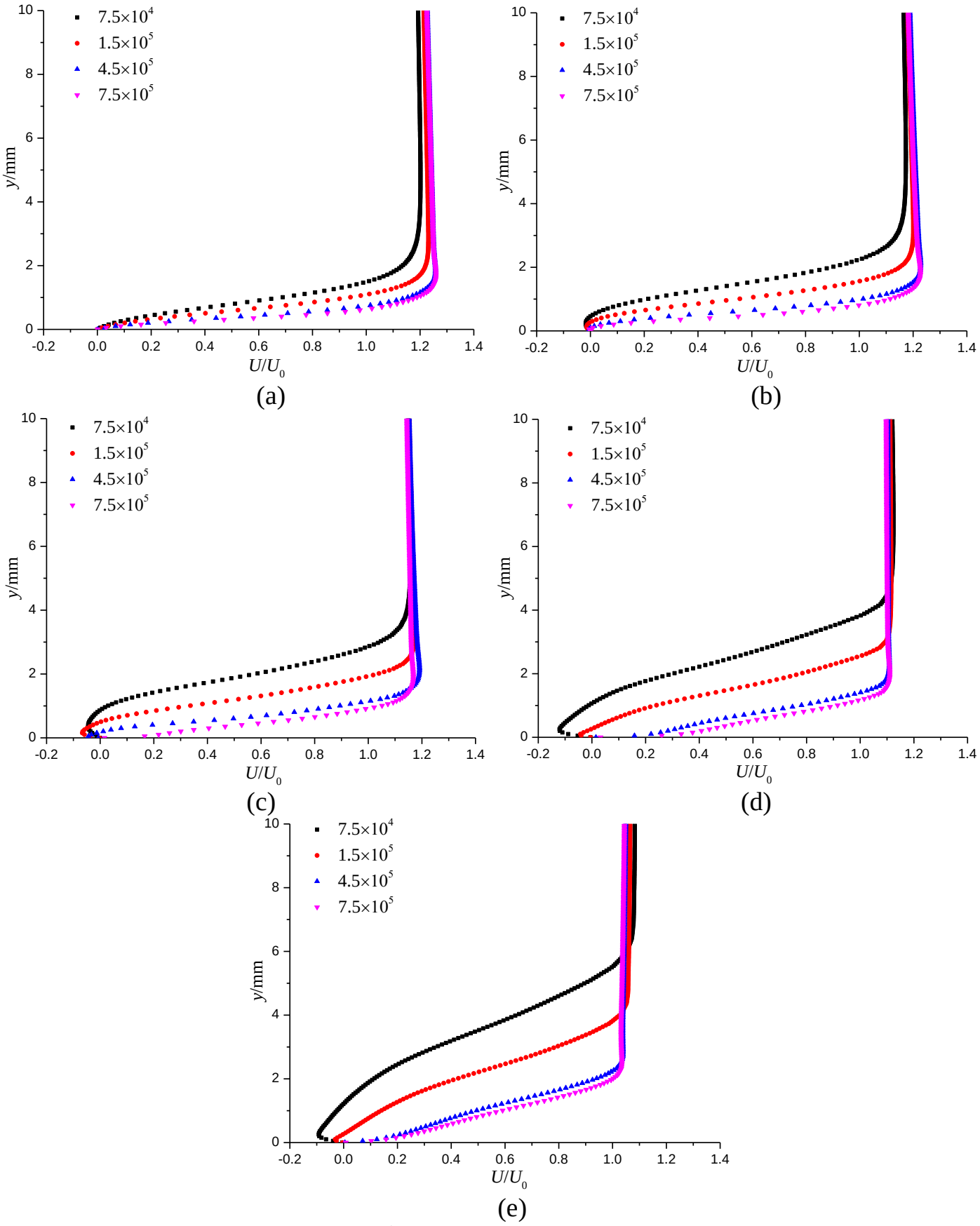

Figure 21 Mean velocity profiles at 2° for various Reynolds numbers. (a) x/c=0.7; (b) x/c=0.8; (c) x/c=0.85; (d) x/c=0.9; (e) x/c=0.95.

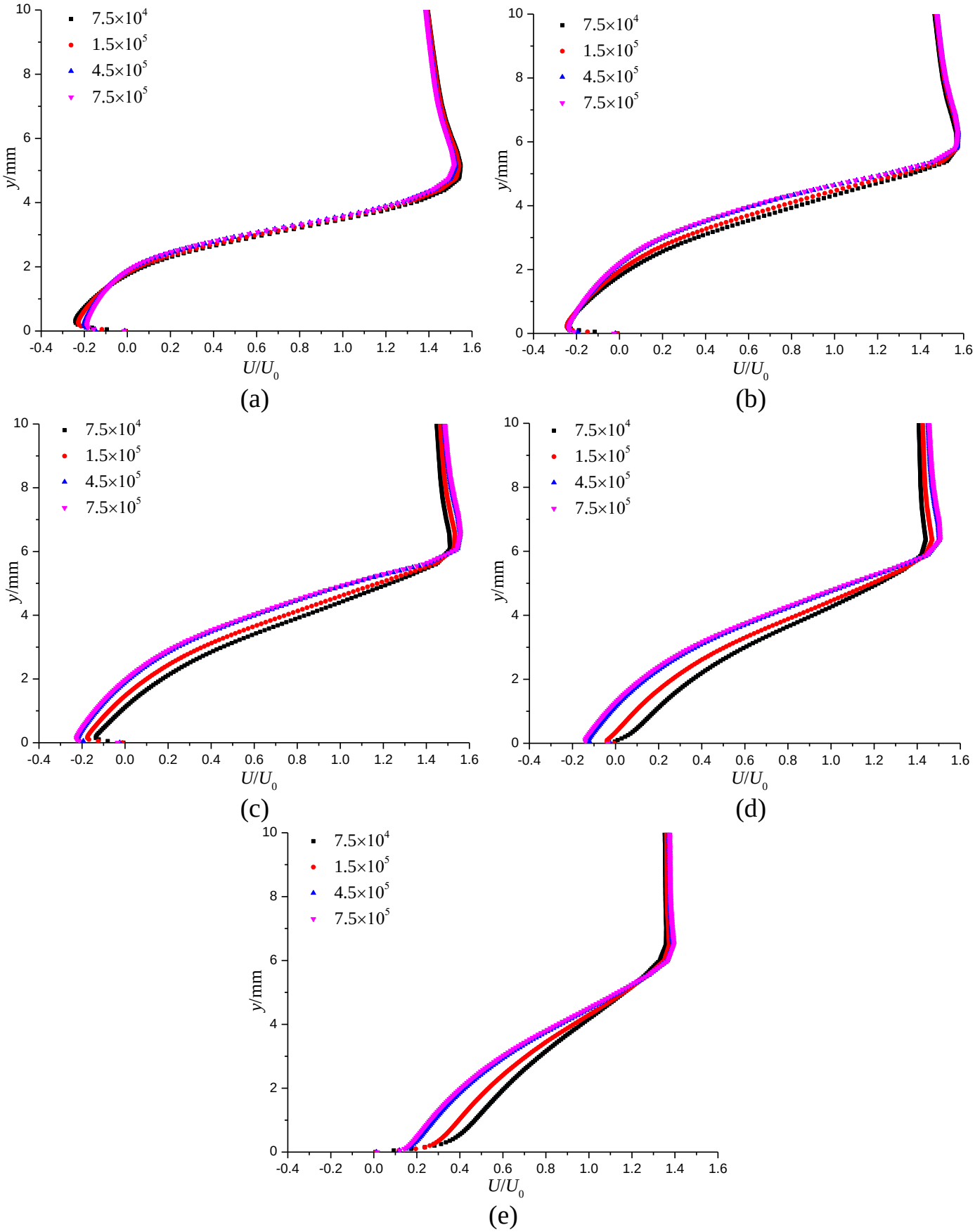

Figure 22 Mean velocity profiles at 8° for various Reynolds numbers. (a) x/c=0.05; (b) x/c=0.1; (c) x/c=0.2; (d) x/c=0.3; (e) x/c=0.4.

5. Conclusion and future work

The transitional flows over the forward and reversed hydrofoils are investigated numerically using the SST γ-$\widetilde{Re}_{\theta t}$ transition model. The effect of inflow turbulence condition, turbulence model and Reynolds number on the transition locations are discussed in detail. Some important conclusions are drawn as follows:

(1) It shows that the inflow turbulence intensity has almost no influence on the transition and hydrodynamics performance, but the effect of eddy viscosity ration can't be neglected. It is observed that the transition moves upstream as the eddy viscosity ratio increases, changing the pressure coefficients both on the suction and pressure sides, which leads to the dramatical modification of the globe performance.

(2) Compared with the original SST k-ω model, the mean velocity profiles and LSB structures are well predicted by SST γ- $\widetilde{Re}_{\theta t}$ transition model. Besides, the hydrofoil performance predicted by the transition model agrees better with the experiments, especially at small attack angles. With the incidence changing from -5° to 14°, the transition on the pressure side moves towards the trailing edge while it changes from the trailing edge to the leading edge on the suction side.

(3) When the hydrofoil is placed reversely, the performance is worse than that for the forward hydrofoil, especially after 2° where the large-scale RDV appears near the leading edge. The movement of the transition is very similar with the forward hydrofoil, but it is located near the leading edge at 5°, which is earlier than forward hydrofoil (at 6°). Additionally, there is a recirculation region of the vortex pair near the trailing edge and it will integrate into a large-scale vortex structure, which moves towards the upper surface, as the incidence increases. With the increase of the Reynolds number, the flow separation and reattachment are delayed when the RDV is located near the leading edge, but for 4.5×10^5, the RDV has the shortest length at -5°, characterized by the earlier reattachment point. Simultaneously, the Reynolds number also has great impact on the flow pattern near the trailing edge where the transition mixes with the flow separation flows, especially under low-Reynolds-number condition.

Due to the limitations of RANS models in predicting the massive separation flows, especially for the reversed hydrofoil where the separation-induced transition near the sharp leading edge occurs more earlier, it is urgent to use the LES methodology to reveal the internal structure and turbulence characteristic of RDV. The influence of mesh and numerical error can be evaluated by some approaches [45-46], and various flow conditions, involving the incidence, inflow turbulence condition and Reynolds number, will be also considered in the future work.

Acknowledgement

This work was financially supported by China Scholarship Council.

References

[1] Critzos, C. C., Heyson, H. H., & Boswinkle Jr, R. W. (1955). Aerodynamic characteristics of NACA 0012 airfoil section at angles of attack from 0 deg to 180 deg (No. NACA-TN-3361).

[2] Lind, A. H., Lefebvre, J. N., & Jones, A. R. (2014). Time-averaged aerodynamics of sharp and blunt trailing-edge static airfoils in reverse flow. *AIAA journal*, *52*(12), 2751-2764.

[3] Simoni, D., Lengani, D., Ubaldi, M., Zunino, P., & Dellacasagrande, M. (2017). Inspection of the dynamic properties of laminar separation bubbles: free-stream turbulence intensity effects for different Reynolds numbers. *Experiments in Fluids*, *58*(6), 66.

[4] Ducoin, A., Loiseau, J. C., & Robinet, J. C. (2016). Numerical investigation of the interaction between laminar to turbulent transition and the wake of an airfoil. *European Journal of Mechanics-B/Fluids*, *57*, 231-248.

[5] Xu, J., Fu, Z., Bai, J., Zhang, Y., Duan, Z., & Zhang, Y. (2018). Study of boundary layer transition on supercritical natural laminar flow wing at high Reynolds number through wind tunnel experiment. *Aerospace Science and Technology*, *80*, 221-231.

[6] Koca, K., Genç, M. S., Açıkel, H. H., Çağdaş, M., & Bodur, T. M. (2018). Identification of flow phenomena over NACA 4412 wind turbine airfoil at low Reynolds numbers and role of laminar separation bubble on flow evolution. *Energy*, *144*, 750-764.

[7] Breuer, M. (2018). Effect of inflow turbulence on an airfoil flow with laminar separation bubble: An LES study. *Flow, Turbulence and Combustion*, *101*(2), 433-456.

[8] Istvan, M. S., & Yarusevych, S. (2018). Effects of free-stream turbulence intensity on transition in a laminar separation bubble formed over an airfoil. *Experiments in Fluids*, *59*(3), 52.

[9] Badrya, C., Govindarajan, B., & Chopra, I. (2018). Basic understanding of unsteady airfoil aerodynamics at low Reynolds numbers (10^4~10^5). In *2018 AIAA Aerospace Sciences Meeting* (p. 2061).

[10] Lian, Y., & Shyy, W. (2007). Laminar-turbulent transition of a low Reynolds number rigid or flexible airfoil. *AIAA journal*, *45*(7), 1501-1513.

[11] Roberts, S. K., & Yaras, M. I. (2006). Effects of surface-roughness geometry on separation-bubble transition. *Journal of Turbomachinery*, *128*(2), 349-356.

[12] Menter, F. R., Langtry, R. B., Likki, S. R., Suzen, Y. B., Huang, P. G., & Völker, S. (2006). A correlation-based transition model using local variables—part I: model formulation. *Journal of turbomachinery*, *128*(3), 413-422.

[13] Menter, F. R., Langtry, R., & Völker, S. (2006). Transition modelling for general purpose CFD codes. *Flow, turbulence and combustion*, *77*(1-4), 277-303.

[14] Langtry, R. B., Menter, F. R., Likki, S. R., Suzen, Y. B., Huang, P. G., & Völker, S. (2006). A correlation-based transition model using local variables—part II: test cases and industrial applications. *Journal of Turbomachinery*, *128*(3), 423-434.

[15] Baltazar, J., Rijpkema, D., & de Campos, J. F. (2018). On the use of the $\gamma-\mathrm{Re}_{\theta t}$ transition model for the prediction of the propeller performance at model-scale. *Ocean Engineering*, *170*, 6-19.

[16] Moran-Guerrero, A., Gonzalez-Gutierrez, L. M., Oliva-Remola, A., & Diaz-Ojeda, H. R. (2018). On the influence of transition modeling and crossflow effects on open water propeller simulations. *Ocean Engineering*, *156*, 101-119.

[17] Lanzafame, R., Mauro, S., & Messina, M. (2013). Wind turbine CFD modeling using a correlation-based transitional model. *Renewable Energy*, *52*, 31-39.

[18] Xu, L., Baglietto, E., & Brizzolara, S. (2018). Extending the applicability of RANS turbulence closures to the simulation of transitional flow around hydrofoils at low Reynolds number. *Ocean Engineering*, *164*, 1-12.

[19] Karasu, İ., Özden, M., & Genç, M. S. (2018). Performance assessment of transition models for three-dimensional flow over NACA4412 wings at low Reynolds numbers. *Journal of Fluids Engineering*, *140*(12), 121102.

[20] Crivellini, A., & D'Alessandro, V. (2014). Spalart–Allmaras model apparent transition and RANS simulations of laminar separation bubbles on airfoils. *International Journal of Heat and Fluid Flow*, *47*, 70-83.

[21] D'Alessandro, V., Montelpare, S., Ricci, R., & Zoppi, A. (2017). Numerical modeling of the flow over wind turbine airfoils by means of Spalart–Allmaras local correlation-based transition model. *Energy*, *130*, 402-419.

[22] Kubacki, S., & Dick, E. (2016). An algebraic model for bypass transition in turbomachinery boundary layer flows. *International Journal of Heat and Fluid Flow*, *58*, 68-83.

[23] Kapsalis, P. C. S., Voutsinas, S., & Vlachos, N. S. (2016). Comparing the effect of three transition models on the CFD predictions of a NACA0012 airfoil aerodynamics. *Journal of Wind Engineering and Industrial Aerodynamics*, *157*, 158-170.

[24] Wang, Y., Li, Y., Xiao, L., Zhang, B., & Li, Y. (2018). Similarity-solution-based improvement of γ-Reθt model for hypersonic transition prediction. *International Journal of Heat and Mass Transfer*, *124*, 491-503.

[25] Liu, J., Xiao, Z., & Fu, S. (2018). Unsteady Transition studies over a pitching airfoil using a k-ω-γ transition model. *AIAA Journal*, *56*(9), 3776-3781.

[26] AlMutairi, J., ElJack, E., & AlQadi, I. (2017). Dynamics of laminar separation bubble over NACA-0012 airfoil near stall conditions. *Aerospace Science and Technology*, *68*, 193-203.

[27] Benton, S. I., & Visbal, M. R. (2019). The onset of dynamic stall at a high, transitional Reynolds number. *Journal of Fluid Mechanics*, *861*, 860-885.

[28] Asada, K., & Kawai, S. (2018). Large-eddy simulation of airfoil flow near stall condition at Reynolds number 2.1× 106. *Physics of Fluids*, *30*(8), 085103.

[29] Visbal, M. R., & Garmann, D. J. (2017). Analysis of dynamic stall on a pitching airfoil using high-fidelity large-eddy simulations. *AIAA Journal*, 46-63.

[30] Guillaud, N., Balarac, G., & Goncalvès, E. (2018). Large eddy simulations on a pitching airfoil: Analysis of the reduced frequency influence. *Computers & Fluids*, *161*, 1-13.

[31] Lind, A. H., & Jones, A. R. (2015). Vortex shedding from airfoils in reverse flow. *AIAA Journal*, *53*(9), 2621-2633.

[32] Lind, A. H., Lefebvre, J. N., & Jones, A. R. (2013). Experimental investigation of reverse flow over sharp and blunt trailing edge airfoils. In *31st AIAA Applied Aerodynamics Conference* (p. 3036).

[33] Lind, A. H., Smith, L. R., Milluzzo, J., & Jones, A. R. (2015). Reynolds number effects on airfoils in reverse flow. In *53rd AIAA Aerospace Sciences Meeting* (p. 1973).

[34] Lind, A. H., Smith, L. R., Milluzzo, J. I., & Jones, A. R. (2016). Reynolds number effects on rotor blade sections in reverse flow. *Journal of Aircraft*, *53*(5), 1248-1260.

[35] Lind, A. H., & Jones, A. R. (2016). Unsteady airloads on static airfoils through high angles of attack and in reverse flow. *Journal of Fluids and Structures*, *63*, 259-279.

[36] Marchand, J. B., Astolfi, J. A., & Bot, P. (2017). Discontinuity of lift on a hydrofoil in reversed flow for tidal turbine application. *European Journal of Mechanics-B/Fluids*, *63*, 90-99.

[37] Lind, A. H., & Jones, A. R. (2016). Unsteady aerodynamics of reverse flow dynamic stall on an oscillating blade section. *Physics of Fluids*, *28*(7), 077102.
[38] Smith, L. R., & Jones, A. R. (2019). Measurements on a yawed rotor blade pitching in reverse flow. *Physical Review Fluids*, *4*(3), 034703.
[39] Hodara, J., Lind, A. H., Jones, A. R., & Smith, M. J. (2016). Collaborative investigation of the aerodynamic behavior of airfoils in reverse flow. *Journal of the American Helicopter Society*, *61*(3), 1-15.
[40] Clifford, C. J., Singhal, A., & Samimy, M. (2014). A study of physics and control of a flow over an airfoil in fully-reverse condition. In *52nd Aerospace Sciences Meeting* (p. 1265).
[41] Menter, F., Kuntz, M., & Langtry, R. (2003). Ten years of industrial experience with the SST turbulence model. *Turbulence, Heat and Mass Transfer*, *4*, 625-632.
[42] Ducoin, A., Astolfi, J. A., & Gobert, M. L. (2012). An experimental study of boundary-layer transition induced vibrations on a hydrofoil. *Journal of Fluids and Structures*, *32*, 37-51.
[43] Ducoin, A., & Young, Y. L. (2013). Hydroelastic response and stability of a hydrofoil in viscous flow. *Journal of fluids and structures*, *38*, 40-57.
[44] Delfin, P. L., Deniset, F., & Astolfi, J., A. (2014). Effect of the laminar seperation bubble induced transition on the hydrodynamic performance of a hydrofoil. *European Journal of Mechanics-B/Fluids*, *46*, 190-200.
[45] Long, Y., Long, X. P., Ji, B., & Xing, T. (2019). Verification and validation of large eddy simulation of attached cavitating flow around a Clark-Y hydrofoil. *International Journal of Multiphase Flow*, *115*, 93-107.
[46] Celik, I. B., Cehreli, Z. N., & Yauvz, I. (2005). Index of resolution quality for large eddy simulation. *Journal of Fluids Engineering*, *127*(5), 949-958.